Title
PION-PION RESONANCES FROM PION-NUCLEON INELASTIC INTERACTIONS

Permalink
https://escholarship.org/uc/item/1cv3h7d4

Author
Guiragossian, Zaven G.T.

Publication Date
1963-08-13

University of California

Ernest O. Lawrence Radiation Laboratory

PION-PION RESONANCES FROM PION-NUCLEON INELASTIC INTERACTIONS

Berkeley, California

DISCLAIMER

UNIVERSITY OF CALIFORNIA

Lawrence Radiation Laboratory
Berkeley, California

Contract No. W-7405-eng-48

PION-PION RESONANCES FROM
PION-NUCLEON INELASTIC INTERACTIONS

Zaven G. T. Guiragossián

August 13, 1963

PION-PION RESONANCES FROM
PION-NUCLEON INELASTIC INTERACTIONS

Contents

PION-PION RESONANCES FROM
PION-NUCLEON INELASTIC INTERACTIONS

Zaven G. T. Guiragossián

Lawrence Radiation Laboratory
University of California
Berkeley, California

August 13, 1963

ABSTRACT

We used the Lawrence Radiation Laboratory's 72-Inch Hydrogen Bubble Chamber with a 3.3-BeV/c π^- beam to study the pion-pion system in π-p interactions. Events were analyzed by means of the FOG-CLOUDY-FAIR data reduction system. We identified 532 events to be (1) $\pi^- + p \rightarrow \pi^- + \pi^+ + n$ ($\pi^-\pi^+$ system, T = 0, 1, 2), and 365 events to be (2) $\pi^- + p \rightarrow \pi^- + \pi^0 + p$ ($\pi^-\pi^0$ system, T = 1, 2).

If high-energy interactions are dominated by a Regge pole having the quantum numbers of the vacuum (T = 0, J parity even) then such a pole should manifest itself in the physical region as a $\pi\pi$ resonance in the T = 0, J = 2 state, at a $\pi\pi$ barycentric energy of ω = 1000 to 1300 MeV.

Our distribution in ω for reactions (1) and (2) is strongly peaked at 775 MeV, which accounts for the T = 1 ρ^0 and ρ^- mesons, respectively. Moreover, reaction (1) has a second peak at a central value of 1250 MeV. We discuss the possibility that this peak is the T = 0, J = 2 $\pi\pi$ resonance mentioned above.

The resonant behaviors of these peaks are studied by means of the decay angular distribution of the final π^- in the $\pi\pi$ barycentric system.

Dalitz plots for both reactions are constructed in order to study possible N^* resonances. Evidence for the $N^*_{3/2}(1238)$ resonance is found in the π^0-p system, whereas N^* resonances in other states seem to be absent.

PION-PION RESONANCES FROM
PION-NUCLEON INELASTIC INTERACTIONS*

Zaven G. T. Guiragossián†

Lawrence Radiation Laboratory
University of California
Berkeley, California

August 13, 1963

I. INTRODUCTION

Motivated by recent theoretical predictions, we have studied the pion-pion barycentric energy spectrum from $\pi^- + p$ inelastic scattering. The data were obtained by using the Lawrence Radiation Laboratory (LRL) 72-Inch Hydrogen Bubble Chamber with a 3.3 BeV/c π^- beam produced by the Bevatron. The reactions studied were

$$\pi^- + p \rightarrow \pi^- + p, \tag{I-1}$$

$$\pi^- + p \rightarrow \pi^- + p + \pi^0, \tag{I-2}$$

and $$\pi^- + p \rightarrow \pi^- + \pi^+ + n. \tag{I-3}$$

In reactions (I-2) and (I-3) the square of the pion-pion barycentric energy, ω^2, ranges from $4 \leq s \leq 156$, where $s = \omega^2/m_\pi^2$. The $\pi^-\pi^0$ and $\pi^-\pi^+$ charge states have been studied. These have isotopic spins $T = 1, 2$, and $T = 0, 1, 2$, respectively.

A peripheral-collision method for experimentally isolating the pion-pion interaction from the pion-nucleon collision was suggested by Chew and Low.[1] This is an extrapolation procedure which requires more data than are available. Therefore, our evidence for pion-pion resonances is based solely on the pion-pion barycentric-energy spectrum in the physical region. The assumption of a peripheral-collision mechanism implies that small momentum transfers to the nucleon should predominate. Such a predominance has been observed, indicating that for the bulk of our data the collisions are peripheral and the pion-nucleon final-state interactions are relatively weak. In this connection, the high energy of our experiment is useful because the minimum value of the nucleon momentum transfer, Δ^2 min, remains small over a wide range of s.

A pion-pion resonant state with $J = 1$, $T = 1$ was first theoretically predicted in order to explain the isotopic-vector part of the nucleon form factor.[2] In a later evaluation,[3] it was predicted that the position of the

resonance would be at $s = \omega^2/\mu^2 = 22$. Since then, several experiments have shown conclusive evidence for a pion-pion resonance in the T = 1 state at a mass value of 740 to 770 MeV.[4,5,6] This is known as the ρ meson.

Recent theoretical arguments based on Regge-pole trajectories suggest the existence of a number of other $\pi\pi$ resonances in the mass region studied here.[7,8,9] The most interesting of these is a T = 0, J = 2 resonance at a mass value of 1000 to 1300 MeV. Along with recent experiments[10,11,24] we present evidence for a $\pi\pi$ resonance in this state which may fit naturally into the pattern of Regge trajectories.

II. EXPERIMENTAL DETAILS

A. Beam Geometry

The geometry of the beam is illustrated in Fig. 1.   The beam was designed by Professor M. L. Stevenson for the initial test run of the 72-Inch Hydrogen Bubble Chamber.

Negative pions were produced at zero degrees to the circulating proton beam incident on a beryllium target.   These pions were deflected 14.49 deg by the Bevatron field and passed through a thin window in the vacuum tank. The beam passed successively through the collimators C_1 and C_2 and the 4-in. quadrupole triplets 4Q1 and 4Q2 as shown in Fig. 1.   An analyzing magnet H, bent the 3.3-BeV/c beam 9.08 deg into the 72-Inch Hydrogen Bubble Chamber.

B. Scanning and Selection of Events

The π^- film was scanned in three views yielding 3610 measureable frames with an average intensity of 20 beam tracks per frame.   The scanners recorded all two-prong events whose vertices fell between the first and last fiducial marks on the top glass of the chamber.   Vertices associated with strange-particle production were not considered.   Beam tracks entering with an angle of more than 4 deg with respect to the general stream of tracks were rejected.   The resulting sample of two-prong events constituted the candidates for the three reactions given by Eqs. (I-1), (I-2), and (I-3).   Figure 2 shows a representative frame.

The curvature of each track was recorded and a note was made when the positive particle stopped in the liquid.   The apparent ionization of the positive track was estimated with respect to the beam track.   In this way, a tentative distinction was made between protons and positive pions.

After these events were measured, we scanned the frames for the second time having the momenta and angles of the tracks at hand.   The apparent ionization was corrected using dip angle, and this was compared with the ionization to be expected for pions and protons.   The positive tracks were identified as protons or positive pions up to a momentum limit of 1.0 BeV/c. Thus, a separation was made between the candidates to the reactions (I-2) and (I-3) up to the above momentum limit.   Dynamically, no inelastic event
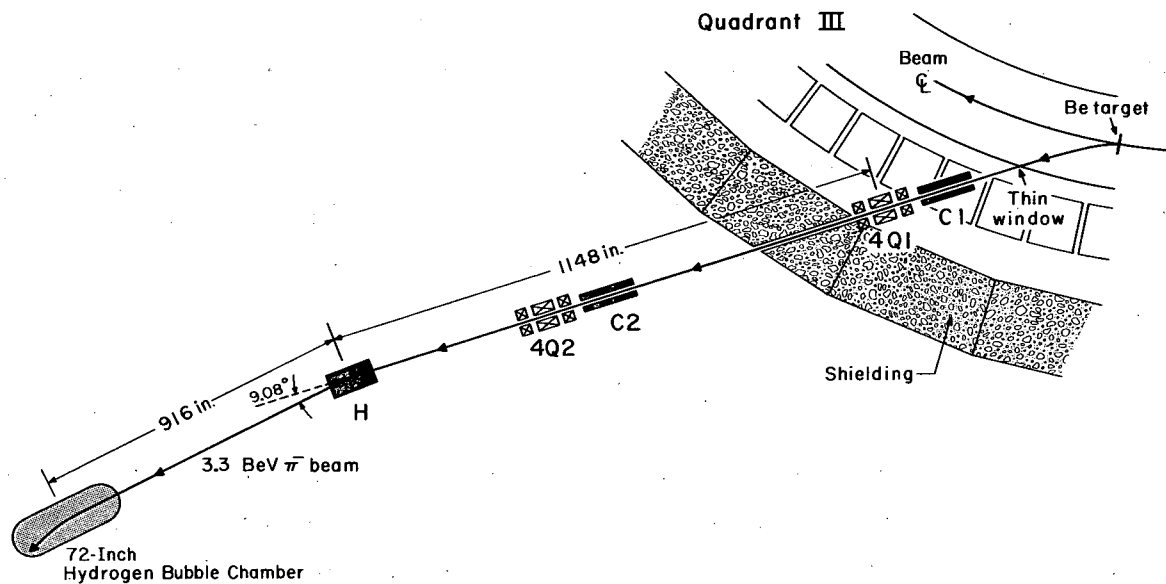
Fig. 1.   The beam geometry.
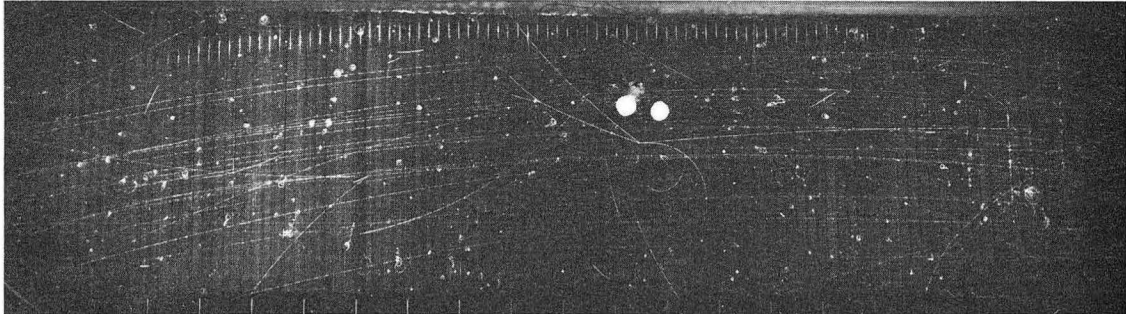
ZN-3898

Fig. 2. 3.3-BeV/c π^- on the 72-Inch Hydrogen Bubble
Chamber.

can have an angle of more than 80 deg between the incoming π^- and outgoing
proton tracks. Whenever such an angle appeared it indicated reaction (I-1).
New events found on the second scan were submitted for measurement.

C. Measurement

There were 6160 events submitted for measurement on a semi-automatic
measuring microscope adapted to permit simultaneous observation of two
views from the bubble chamber cameras. Figure 3 is a photograph of the
general arrangement. Figure 4 shows the coordinate system for track meas-
urement. The method of measurement consists in determining the coordinates
of a track at several points in both views by means of the digitized microscope.
This information is automatically card-punched and transmitted to the digital
computer, which is programmed to spatially reconstruct the tracks.

D. Data Reduction

The measured events were analyzed on the IBM 7090 Computer using
the FOG-CLOUDY-FAIR data reduction system.[12, 13] A 7.5-deg rotation from
the camera axis to the magnetic field at the center of the track was made to
account for the 72-Inch Hydrogen Bubble-Chamber geometry. Then the spatial
points were fitted to a second-order polynomial.

Figure 5 shows the FOG-CLOUDY-FAIR data reduction chain. Events
were spatially reconstructed and stored on the FOG library tapes. Here, the
momenta and the angles of tracks were computed. Errors were assigned
based on multiple Coulomb scattering and estimated measurability. Whenever
an identified positive particle came to rest in the chamber, the momentum
computed from the range-energy relation was used according to the mass
assignment.

Beam tracks were extrapolated to the chamber-entrance position, where
the α_E and β_E angles were evaluated. Figures 6 and 7 show the distribution
in α_E and β_E of these tracks. These distributions were made for tracks with
lengths $L \geqslant 60$ cm. With these distributions, the beam-acceptance criteria
were defined to be 87.0 deg $< \alpha_E <$ 93.5 deg, and 2.0 deg $< \beta_E <$ 9.5 deg. Tracks
of all lengths were then used, consistent with the above criteria.

In order to define a "good measurement" criterion for each track, the
five worst digitized points deviating from the fitted curve of each track are

ZN-3899

Fig. 3. Photograph of the general arrangement for the
semi-automatic measuring microscope. (A) Track-
number window; (B) View-number window; (C) Fixed-
information panel; (D) Microscope (15X); (E) Film
platen, for simultaneous observation of views 1 and 2
of the 72-Inch Hydrogen Bubble Chamber; (F) IBM 026
card punch; (G) X-motion datax (1 part in 10^5) encoder;
(H) Y-motion drive; (I) Brower measuring engine;
(J) Power supply; (K) Transistorized punch control;
(L) Decoders; (M) Scan cards.
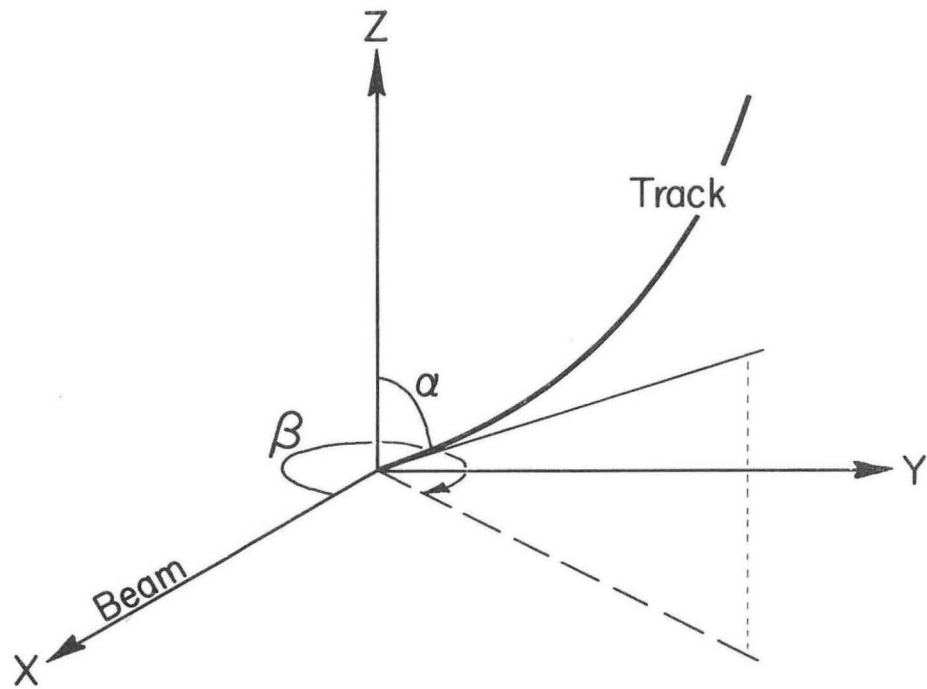
Fig. 4. The coordinate system for track measurement.

MU-18491

FOG - CLOUDY - FAIR
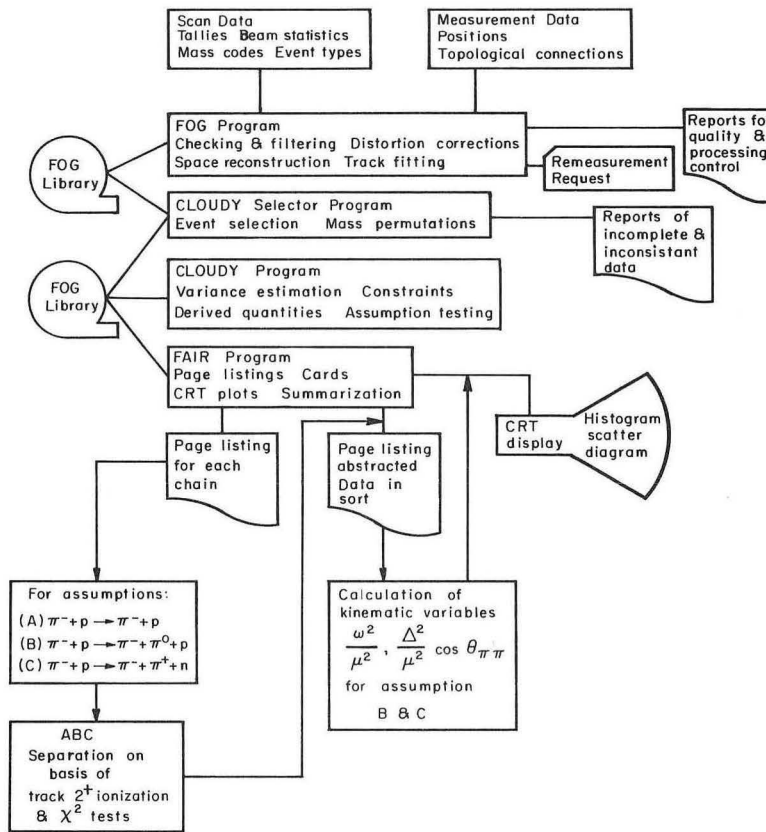
Data reduction system

Fig. 5.   FOG-CLOUDY-FAIR data reduction chain.
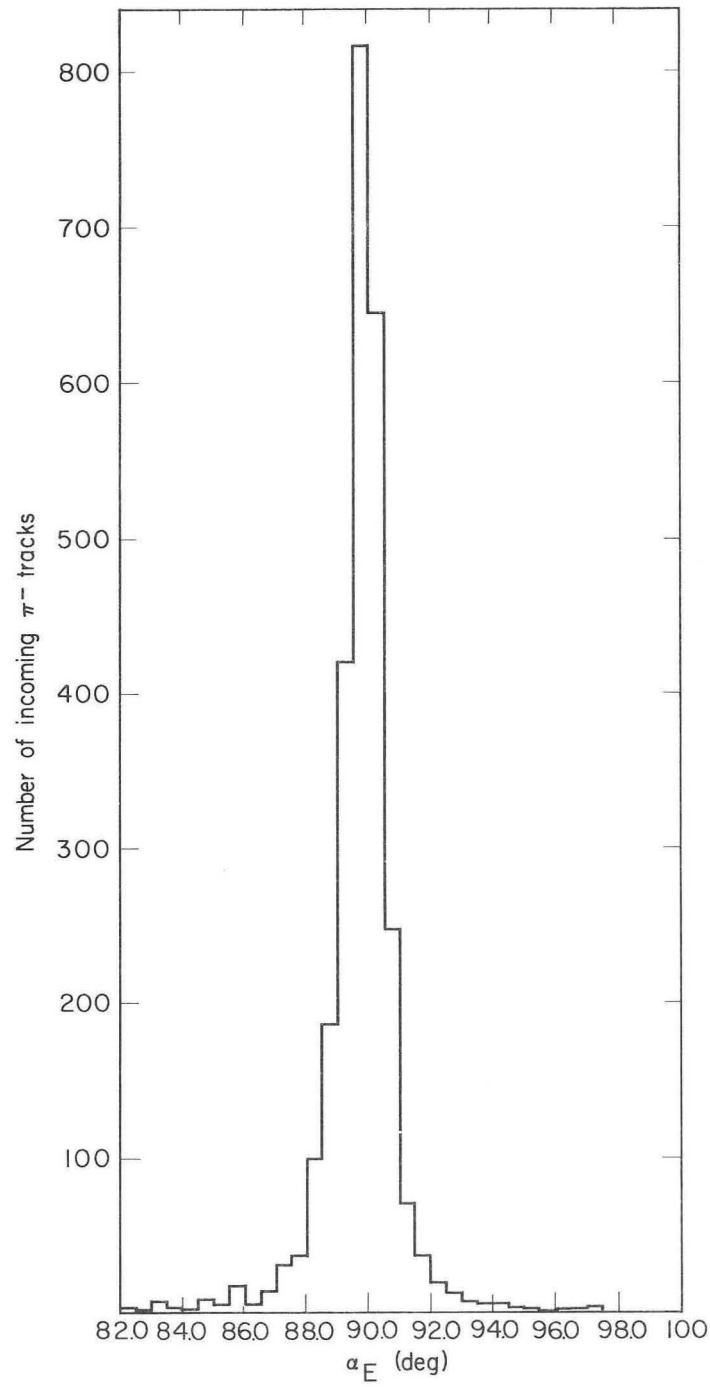
MUB-1697

Fig. 6. Distribution in α_E, the dip angle of beam tracks
extrapolated to the chamber-entrance position, for
measured tracks of length L > 60 cm.

Fig. 7. Distribution in β_E, the azimuthal angle of beam
         tracks extrapolated to the chamber-entrance position,
         for measured tracks of length L > 60 cm.

considered. After neglecting the point with the greatest deviation, the re-
maining four points are used to define an average deviation:

$$\Delta\eta = \frac{1}{4} \sum_{i=2}^{5} \left| \Delta x_i \right| ,$$

where Δx_i is the deviation of the digitized point normal to the fitted curve.
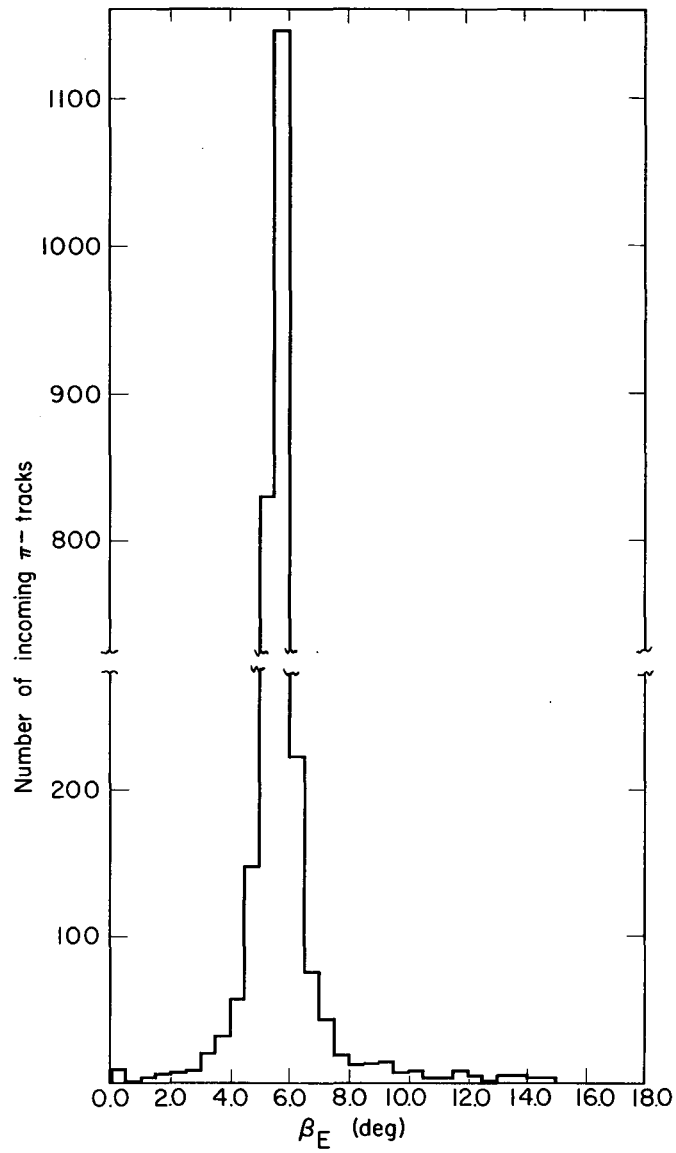Figure 8 shows the distribution in $\Delta\eta$ of events identified as candidates to
reaction (I-3). The top and center distributions are for the beam and scat-
tered π^- tracks, the bottom distribution is for the identified π^+ tracks.

Based on these distributions, limits of "good measurability" are impos-
ed on the entire data. Thus, for all π^- beam tracks we accept $\Delta\eta_0 \leq 0.030$ cm,
for π^- scattered tracks $\Delta\eta_1 \leq 0.035$ cm, and for π^+ or proton tracks
$\Delta\eta_2 \leq 0.040$ cm.

In order to verify the beam-momentum value of 3.3 BeV/c as defined by
the beam geometry, a momentum distribution of measured beam tracks is
made. All beam tracks of length $L > 60$ cm satisfying the entrance dip and
azimuthal angle criteria, and having $\Delta\eta_0 \leq 0.030$ cm, were accepted. Figure 9
illustrates the beam-momentum distribution using the above criteria. From
this a central value of 3.30 ± 0.10 BeV/c is obtained. This value with its un-
certainty was assigned to all the beam tracks through the CLOUDY kinematical-
constraint program.

For each event, the mass permutations relevant to reactions (I-1), (I-2),
and (I-3) were assigned to the CLOUDY program. Figure 10 and Figure 11
illustrate the two-body and three-body kinematical constraints, compatible
with energy and momentum conservation at each vertex. Here, X_i and X_i^m
are the best values and the measured values of the nine parameters, respec-
tively. The α_i's are the Lagrange multipliers to the constraining functions,
the F_i's. The program minimizes M using the partial derivatives $\partial F/\partial X_i$,
and the process is iterated several times. The minimum value of M occurs
when all the F's converge to zero, whereby M becomes a χ^2 test for the good-
ness of fit for each assumption.

E. Identification of Reactions

Events arriving from the CLOUDY kinematical-constraints program
were separated on the basis of the positive-track ionization information up to
a momentum value of 1.0 BeV/c.
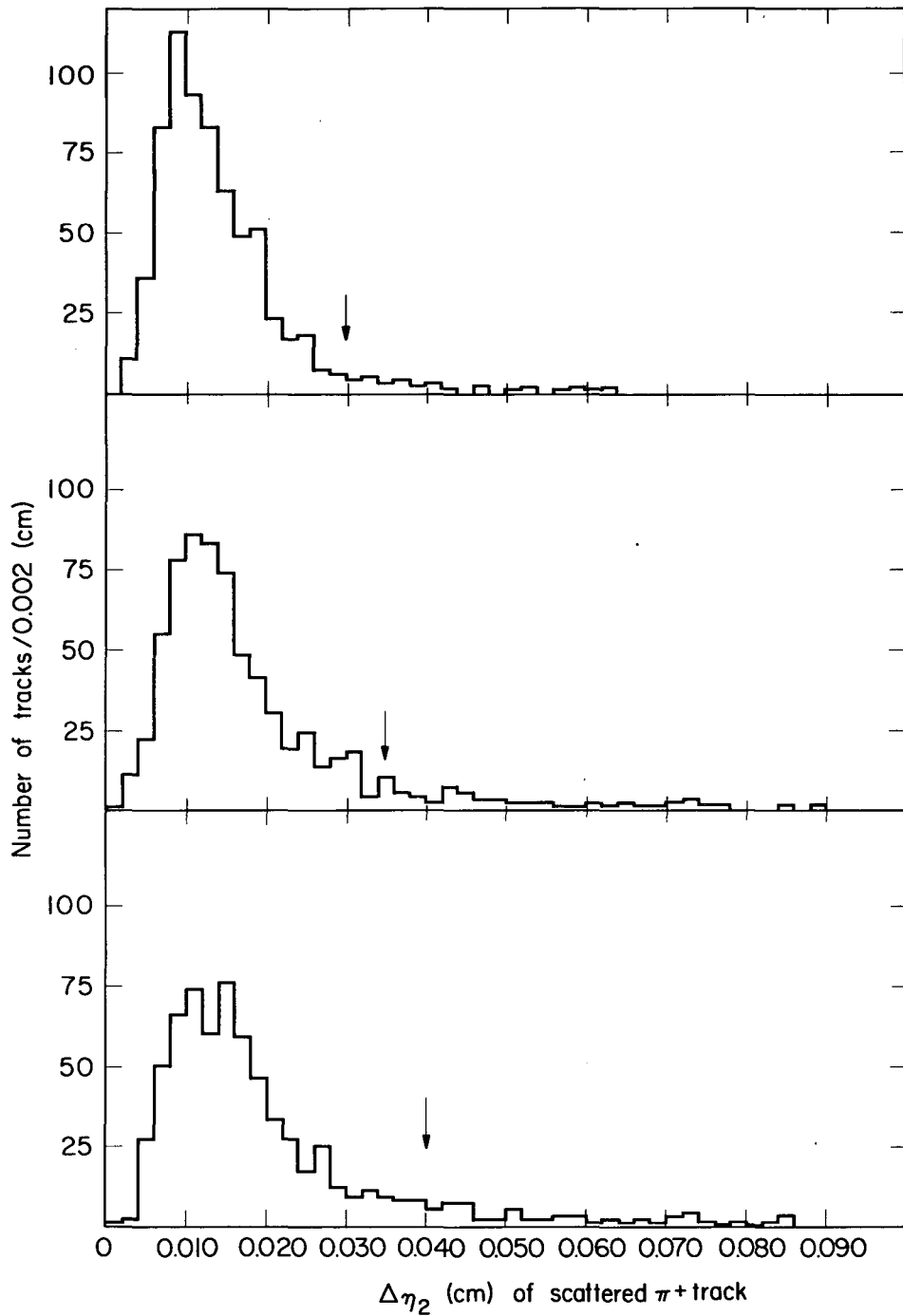
Fig. 8.   Distribution in $\Delta\eta$: top, for π^- beam tracks;
center, for π^- scattered tracks; and bottom, for
identified π^+ tracks.

MUB-1698
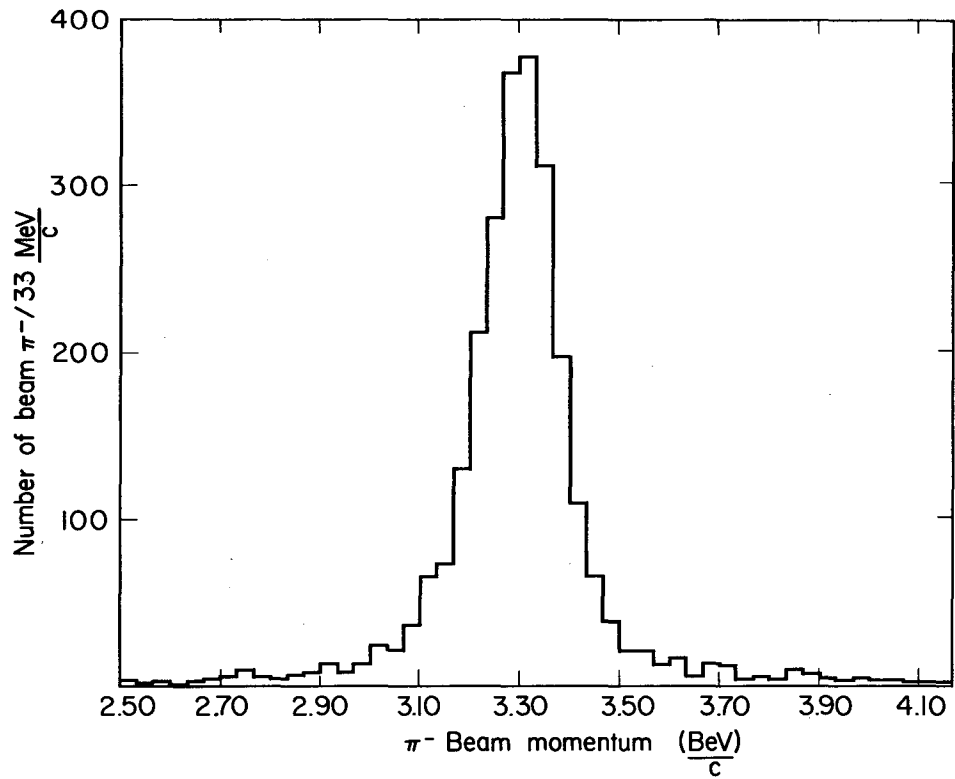
MU-30056

Fig. 9. Momentum distribution of beam tracks of measured
length L > 60 cm.
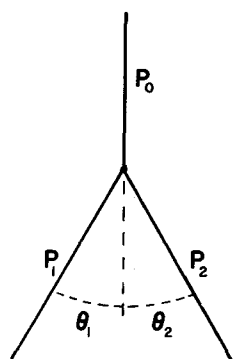
Constraining   Functions

$$F_1 = P_1 \cos \theta_1 + P_2 \cos \theta_2 - P_0$$

$$F_2 = P_1 \sin \theta_1 + P_2 \sin \theta_2 \cos (\phi_2 - \phi_1)$$

$$F_3 = \begin{vmatrix} \lambda_0 & \mu_0 & \nu_0 \\ \lambda_1 & \mu_1 & \nu_1 \\ \lambda_2 & \mu_2 & \nu_2 \end{vmatrix}$$

$$F_4 = E_1 + E_2 - E_0 - M_{TARGET}$$

Constraining   Equation

$$M(x_i, \alpha_j) = \sum_{i=1}^{9} \frac{(x_i - x_i^m)^2}{u_i} + 2 \sum_{j=1}^{4} \alpha_j F_j$$

MU − 21158

Fig. 10.   Two-body kinematical constraints.
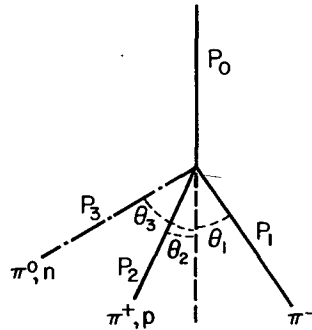
Constraining Functions

$$F_1 = \sum_{i=1}^{3} P_i \, \lambda_i - P_0 \, \lambda_0$$

$$F_2 = \sum_{i=1}^{3} P_i \, \mu_i - P_0 \, \mu_0$$

$$F_3 = \sum_{i=1}^{3} P_i \, \nu_i - P_0 \, \nu_0$$

$$F_4 = \sum_{i=1}^{3} E_i - E_0 - M_p$$

$$\cos \theta_i = \lambda_i \, \lambda_0 + \mu_i \, \mu_0 + \nu_i \, \nu_0$$

$$\lambda_i = \sin \alpha_i \cos \beta_i$$
$$\mu_i = -\sin \alpha \, \sin \beta_i$$
$$\nu_i = \cos \alpha_i$$

$$E_i = \sqrt{P_i^2 + M_i^2}$$

Constraining Equation

$$M(x_i, \alpha_j) = \sum_{i=1}^{9} \frac{(x_i - x_i^m)^2}{u_i} + 2 \sum_{j=1}^{4} \alpha_j \, F_j$$

Measured Variables

$$x_i^m = \left\{ \alpha_0 \, \beta_0 \, \rho_0 , \; \alpha_1 \, \beta_1 \, \rho_1 , \; \alpha_2 \, \beta_2 \rho_2 \right\}$$

Estimated Variable Errors σ_i , $u_i = \sigma_i^2$

MU-25627

Fig. 11.   Three-body kinematical constraints.

An event was considered to be of reaction type (I-1) if it fit the elastic hypothesis with converging iterations, was coplanar, had a χ^2 value ≤ 20.0, and had a positive-track ionization consistent with the "proton assumption." All such events were removed from the entire sample.

The remaining sample was divided into three categories:

(a) π^+ identified events which fit reaction type (I-3) with a $\chi^2 < 9.0$,

(b) proton identified events which fit reaction type (I-2) with a $\chi^2 < 9.0$, and

(c) positive-track unidentified events which fit reaction types (I-2) and/or (I-3).

The missing neutral masses were computed for all categories by using measured parameter values. These were computed by

$$M^2_{n, \pi^0} = (E^i_{\pi^-} + M_p - E^s_{\pi^-} - E_{\pi^+, p})^2 - (\underset{\sim}{P}^i_{\pi^-} - \underset{\sim}{P}^s_{\pi^-} - \underset{\sim}{P}_{\pi^+, p})^2 ,$$

in which the appropriate mass permutation for each category was used.

Figure 13 shows the missing mass distribution of events from category (a), giving a peak at the neutron mass and another near the $(n + \pi^0)$ mass. The arrows indicate the accepted neutron definition, $0.50 < M^2_n < 1.20$. Similarly, Fig. 14 shows the missing mass distribution of events from category (b), giving a peak at the π^0 mass and an enhancement at the η mass. The arrows here indicate the π^0 definition, $-0.12 < M^2_{\pi^0} < 0.10$.

The above missing mass cuts were then imposed on events in category (c) for a final separation into reaction types (I-2) or (I-3). Figures 12 and 13 are given in terms of M^2_0 instead of M_0, since the missing mass squares are expected to have a Gaussian distribution about M^2_n or $M^2_{\pi^0}$.

Thus, 532 events were identified as reaction (I-3) and 365 events as reaction (I-2); these included 30 ambiguous events which had high momentum transfers to the nucleon. In the following distributions, the 30 ambiguous events participate with half their weight.

Figure 14 shows the χ^2 goodness-of-fit distribution of the finally separated events according to the above criteria.

F. Kinematical Variables

The kinematical variables of interest to the study of $\pi\pi$ interactions were defined by Chew and Low.[1] The interaction diagram considered with the assigned variables is the following:
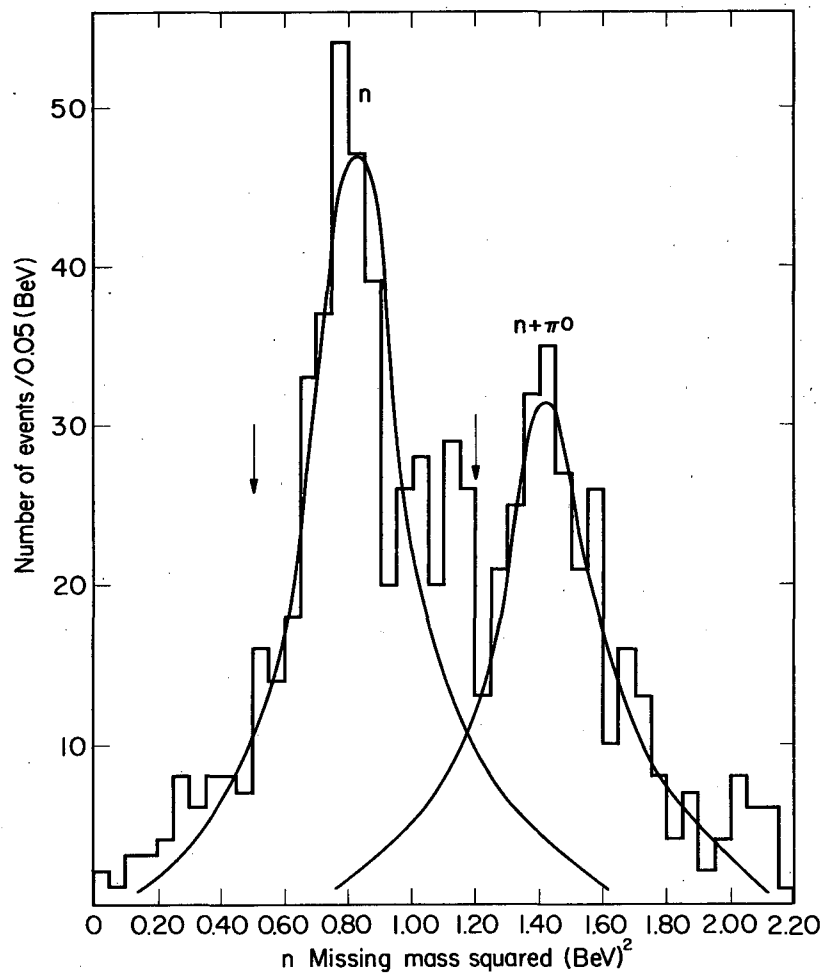
Fig. 12. Missing mass-squares distribution of π^+ identified
events fitting $\pi^- + p \rightarrow \pi^- + \pi^+ + n$. Arrows indicate
the accepted neutron definition.
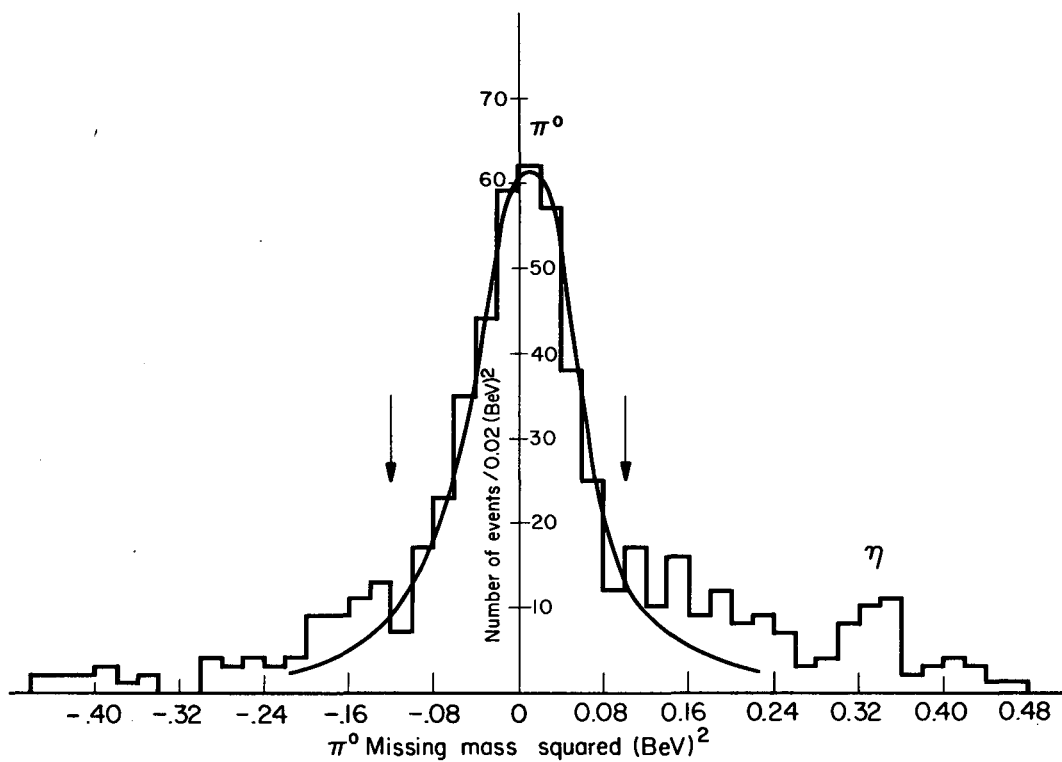
MU-30055

Fig. 13. Missing mass-squares distribution of proton-
identified events fitting $\pi^- + p \rightarrow \pi^- + \pi^0 + p$.
Arrows indicate the accepted π^0 definition.
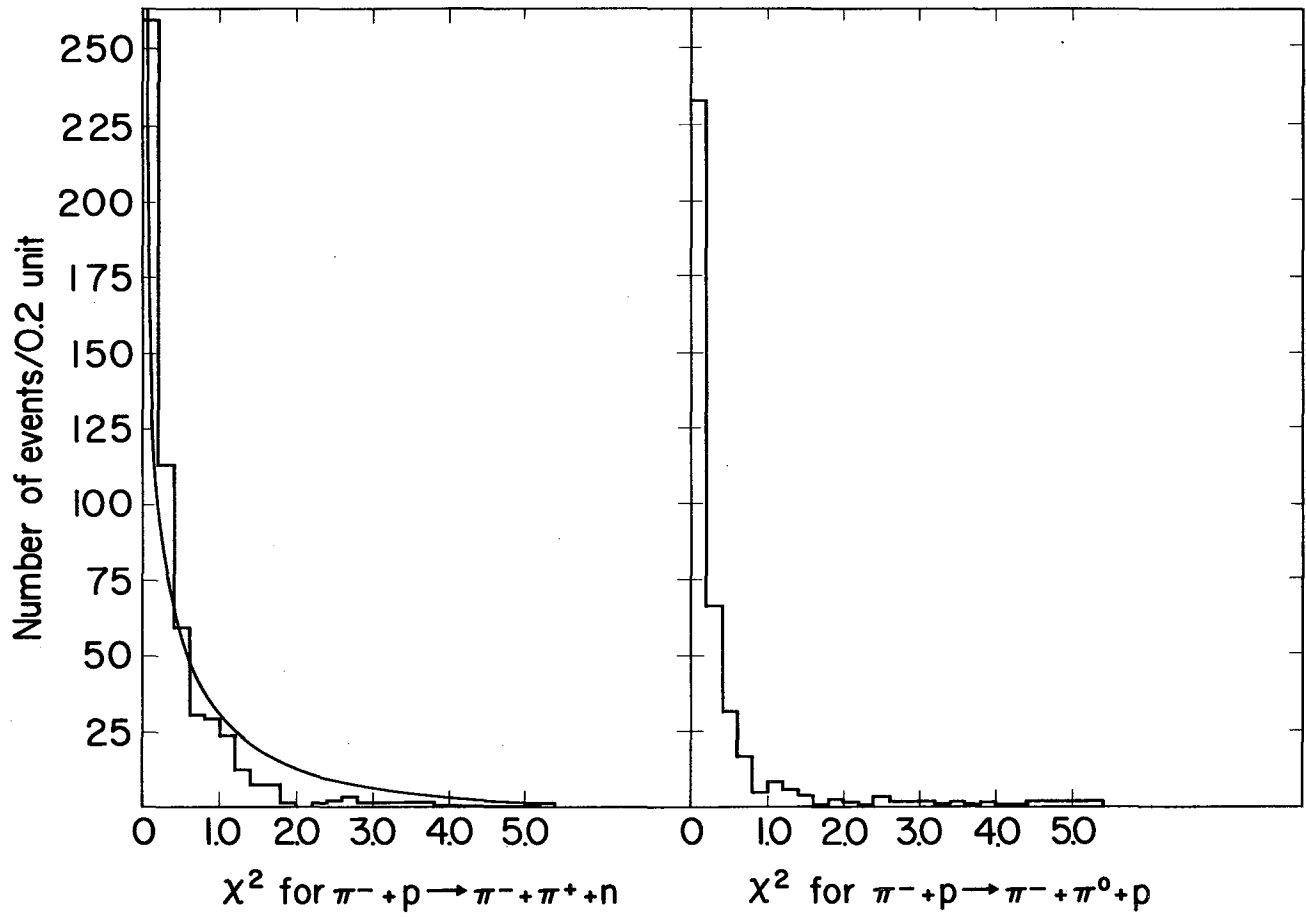
Fig. 14. χ^2 distribution of separated events.
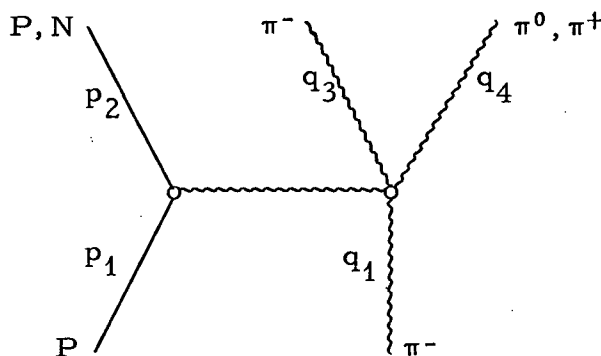
Using 4-vector notation, the invariant-momentum transfer to the nucleon is $\Delta^2 = -(p_1 - p_2)^2$, and the invariant $\pi\pi$ total energy is $\omega^2 = (q_3 + q_4)^2$. Evaluating the variables in the laboratory system for the reaction $\pi^- + p \rightarrow \pi^- + \pi^0 + p$ and using 4-momentum conservation, we obtain

$$\Delta^2 = 2M_p T_{2L}$$

and

$$\omega^2 = 2q_{1L}p_{2L}\cos\theta_{2L} + m_\pi^2 - \Delta^2 - 2\omega_{1L}T_{2L},$$

where T_{2L} is the recoil-proton kinetic energy, θ_{2L} is the proton scattering angle with respect to the beam pion, and ω_{1L} is the beam-pion total energy.

Another variable of interest is the angle between the beam and scattered π^- in the barycentric system of the final pions, $\theta_{\pi\pi}$. This is obtained by evaluating the invariant inner product $q_1 \cdot q_3$ both in the laboratory and in the $\pi\pi$ barycentric systems.

We have

$$q_1 \cdot q_3 = \omega_{1L}\omega_{3L} - q_{1L}q_{3L}\cos\theta_{3L} = \omega_{1B}\omega_{3B} - q_{1B}q_{3B}\cos\theta_{\pi\pi},$$

where

$$\omega_{1B} = (\omega^2 + \Delta^2 + m_{\pi^-}^2)/2\omega, \quad \omega_{3B} = (\omega^2 + m_{\pi^-}^2 - m_{\pi^+,\pi^0}^2)/2\omega,$$

and

$$q_{1B} = (\omega_{1B}^2 - m_{\pi^-}^2)^{1/2}, \text{ and } q_{3B} = (\omega_{3B}^2 - m_{\pi^-}^2)^{1/2},$$

so that we have

$$\cos\theta_{\pi\pi} = \frac{q_{1L}q_{3L}\cos\theta_{3L} + \omega_{1B}\omega_{3B} - \omega_{1L}\omega_{3L}}{q_{1B}q_{3B}}.$$

Here the subscripts L and B refer to the laboratory and the $\pi\pi$ barycentric systems, respectively. Similar expressions are used for the reaction $\pi^- + p \rightarrow \pi^- + \pi^+ + n$.

During the data-reduction chain, the FAIR program abstracts from the CLOUDY library tapes the constrained values of reaction parameters and computes the quantities ω, $s = \omega^2/m_{\pi-}^2$, $t = \Delta^2/m_{\pi-}^2$ and $\cos \theta_{\pi\pi}$ for every event of interest. For each value of ω, an uncertainty $\delta\omega$ is calculated from the error matrix of the constrained variables.

With the events separated into reaction types, a listing of these variables is made for each reaction and submitted to CRT display—automatic electronic histogramming. The FAIR system is programmed to histogram several variables with specified conditions and ranges. Figure 5 displays this final data-reduction stage.

The remaining variable of interest is the Trieman-Yang angle, which is used to test the one-pion-exchange hypothesis in the studied reactions.[14] This angle is defined by

$$\cos \gamma_{TY} = \frac{(\mathbf{p}_1' \times \mathbf{p}_2') \cdot (\mathbf{q}_3' \times \mathbf{q}_4')}{\left| \mathbf{p}_1' \times \mathbf{p}_2' \right| \left| \mathbf{q}_3' \times \mathbf{q}_4' \right|} ,$$

where the momenta are evaluated in the rest frame of the incident π^-. For reasons of programming expediency, this angle was computed outside the FAIR system. FORTRAN reading tapes were abstracted from the FAIR summary tapes containing the variables of interest of finally selected events and these were used with a FORTRAN program[15] to compute the Trieman-Yang angle.

G.   Phase Space

The overall phase space for π-p inelastic interactions is computed in terms of ω^2 and Δ^2. By using the relation

$$\omega^2 = \left(\omega_{1L} - \frac{\Delta^2}{2M_p} \right)^2 - q_{1L}^2 + 2q_{1L}p_{2L} \cos \theta_{2L} - p_{2L}^2 ,$$

and expressing $p_{2L} = \pm [(\Delta^2/2M_p + M_p)^2 - M_p^2]^{1/2}$, the dependence of Δ^2 on ω^2 for a fixed value of θ_{2L} is obtained:

$$\omega^2 = \left(\omega_{1L} - \frac{\Delta^2}{2M_p} \right)^2 - q_{1L}^2 - \left[\left(\frac{\Delta^2}{2M_p} + M_p \right)^2 - M_p^2 \right] \pm \left[\left(\frac{\Delta^2}{2M_p} + M_p \right)^2 - M_p^2 \right]^{1/2} .$$

Here, the upper limit of ω^2 is $(W - M_p)^2$, where $W^2 = M^2 + m_{\pi^-}^2 + 2M\omega_{1L}$, and we have $W = 2.668$ BeV as the overall π-p barycentric-system total energy for $q_{1L} = 3.32$ BeV/c.

The lower limit of the $\pi\pi$ barycentric system total energy is $2m_{\pi^-}$, so that $4 \leqslant \omega^2/m_\pi^2 \leqslant 156$. Figure 15 shows the entire phase space for the reactions

$$\left. \begin{array}{c} \pi^- + p \to \pi^- + \pi^+ + n + n(\pi^0) \\ \\ \pi^- + p \to \pi^- + \pi^0 + p + n(\pi^0) \end{array} \right\} \quad n = 0, 1, 2, \ldots$$

and

in terms of $t = \Delta^2/m_\pi^2$ for fixed values of θ_{2L}. The maximum phase space is obtained for $\theta_{2L} = 0$ deg. The line for elastic events is at $s = 1$.

The phase space of the interaction as a function of s or t is required in order to make a comparison with the experimental distributions from the respective reactions. The general expression for an element of phase space is

$$d\rho = \delta(q_3^2 - m_\pi^2) \, \delta(q_4^2 - m_\pi^2) \, \delta(p_2^2 - M_n^2) \, \delta(p_2 + q_3 + q_4 - P_1 - q_1) \, d^4q_3 \, d^4q_4 \, d^4p_2.$$

Expressing this in terms of the $\pi\pi$ barycentric system variables, and integrating over the undesired variables, we obtain

$$d\rho(s, t) = \frac{\pi^2 m_\pi^4}{8M_p q_{1L}} \left[1 - 4/s \right]^{1/2} ds \, dt.$$

Figure 15 gives the graphical $t = t(s)$ or $s = s(t)$ dependences, thus permitting integrations over t or s in the above expression. We have

$$\frac{d\rho(s)}{ds} = \frac{\pi^2 m_\pi^4}{8M_p q_{1L}} \left[1 - 4/s \right]^{1/2} \left[t(s)_{max} - t(s)_{min} \right]$$

and

$$\frac{d\rho(t)}{dt} = \frac{\pi^2 m_\pi^4}{8M_p q_{1L}} \int_4^{s(t)_{max}} \left[1 - 4/s \right]^{1/2} ds.$$

The phase space can also be expressed as a function of ω, multiplied by a resonance factor of the form $N/[(\omega - \omega_r)^2 + (\Gamma/2)^2]$, where ω_r is the resonant dipion energy and Γ is the full width at half maximum. The normalization N is chosen to give unit area to the resonance so that

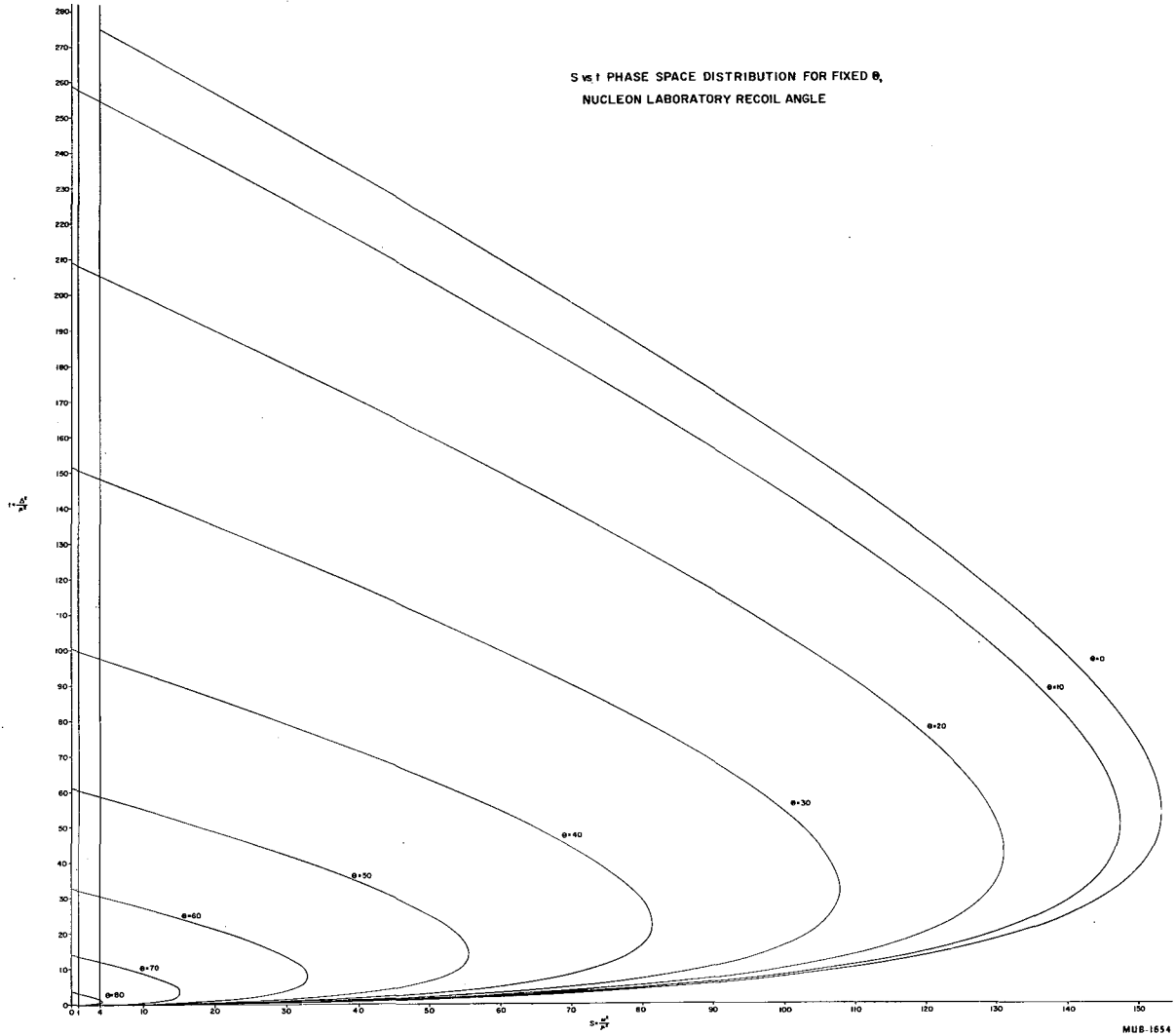$$\int_{\omega_{min}}^{\omega_{max}} N/[(\omega - \omega_r)^2 + (\Gamma/2)^2] \, d\omega = 1.$$

Fig. 15. $s = \omega^2/m_\pi^2$ vs $t = \Delta^-/m_\pi^-$ phase-space limiting
regions for fixed values of θ_{2L}, the recoil-nucleon
laboratory angle. $s = 1$ is the π^-p elastic line.
Beginning with $s = 4$ is the π^-p inelastic-interaction
space for 3.3-BeV π^- laboratory energy.

We have used the LRL ATHOS program[16] to generate phase space and phase space with resonance curves as a function of ω. Other subroutines of the ATHOS program were called to generate Dalitz-plot envelopes and phase-space curves as functions of T_{π}, which is the scattered-pion-reaction center-of-mass kinetic energy.

H. Errors and Experimental Resolution

The FOG and CLOUDY programs assign errors to the measured and constrained track momenta and angles based on track measurability and Coulomb scattering. These are reflected in $\delta\omega$, the uncertainties of the $\pi\pi$ barycentric energy.

If the overall errors have been properly normalized, then the χ^2 goodness-of-fit distribution of both reactions should follow the χ^2 probability distribution for one degree of freedom, $P_1(\chi^2)$, where

$$P_n(m) = \frac{\exp(-m/2)\, m^{(n/2 - 1)}}{2^{n/2}\, \Gamma(n/2)} \ .$$

Figure 14 indicates that the errors have been normalized with a slight over-estimation.

The beam-momentum 3% uncertainty contributes approximately 15 MeV to $\delta\omega$, where $\partial\omega/\partial q_{1L} = [p_{2L} \cos\theta_{2L} - T_{2L}q_{1L}/\omega_{1L}]/\omega$. All remaining error contributions bring $\delta\omega$ to about 35 MeV; accordingly we have chosen to histogram ω in 50-MeV intervals.

III. THEORETICAL CONSIDERATIONS

Chew and Low[1] have suggested a general method to analyze scattering processes on unstable targets. In particular, their method is aimed at extracting the $\pi\pi$ interaction from pion-nucleon inelastic scattering.

The process $\pi + N \rightarrow \pi + \pi + N$, proceeding through the one-pion-exchange mechanism, is illustrated by the diagram in Sec. II-F. Here the scattering amplitude has an isolated pole at $\Delta^2 = -m_\pi^2$, where the residue contains the $\pi\pi$ cross section. Thus, the pion-nucleon cross section is expressed in terms of the pion-pion cross section as

$$\frac{\partial^2 \sigma_{\pi^- p}(\omega^2, \Delta^2)}{\partial \omega^2 \, \partial \Delta^2} \quad \underset{\Delta^2 \to -m_\pi^2}{\lim} \quad \frac{f^2}{2\pi} \frac{\Delta^2/m_\pi^2}{[\Delta^2 + m_\pi^2]^2} \frac{\omega(\omega^2/4 - m_\pi^2)^{1/2}}{q_{1L}^2} \, \sigma_{\pi^0 \pi^-}(\omega^2),$$

so that, in the physical region, the interaction is characterized by a strong enhancement at small values of Δ^2. This gives a test of whether the interaction proceeds according to the above mechanism, or whether it has competing final-state and core interactions.

This extrapolation procedure to determine the $\pi\pi$ cross section requires more data than that available in the present experiment.

A. Regge Poles and Pion-Pion Resonances

There exist several reviews on the occurrence of poles in the analytically continued S matrix for complex angular-momentum values.[17] Rigorously speaking, Regge's results apply to the case of nonrelativistic potential scattering.[18] However, conjectures and attempts have been made to carry the Regge analysis to the case of relativistic strong interactions.[7-9,19,20] We summarize here some of the conclusions relevant to the $\pi\pi$ problem.

The Chew-Frautschi conjecture[7] considers that particles appear as poles $a_T(s)$ of the S matrix, and a particle family may be obtained by tracing the Regge trajectory $\mathrm{Re}\, a_T(s)$ vs s, knowing the slope $a_T'(s)$. Such a trajectory is defined by its intrinsic quantum numbers: isotopic spin T, and J parity. We note that for the case of pions, J parity and the well-known G parity have the same implications.

A given trajectory then, generates particles of the family at values of $\mathrm{Re}\, a_T(s) = J$, where, due to J parity, only alternate J values will be meaningful.

For a given two-body reaction, the potential strength in a given channel is related to the scattering amplitude in the crossed channel through known crossing relations. In such a reaction, a particle on a Regge trajectory can be exchanged if the trajectory has the same intrinsic quantum numbers as that of the crossed channel.

In examining the asymptotic limits of the $\pi\pi$ scattering amplitude, it is found that it behaves as $A^T(t, s) \xrightarrow[t \to \infty]{} t^{a_T(s)} \beta(t)$, where $a_T(s)$ is the extension of angular momentum ℓ to complex values, and $\beta(t)$ is the Regge-pole residue. Moreover, for the cases of T = 0, 1, and 2, it is found that

$$a_{T=0}(0) > a_{T=1}(0) > a_{T=2}(0),$$

with the condition that $a_{T=0}(0) = 1$.

Thus, the potential strength is split in the above order for different values of T, with the Pomeranchuk trajectory (T = 0, J parity even) having the greatest strength. This state can be reached by an even number of pions.

Due to Bose statistics, the $\mathrm{Re}\, a_{T=0}(0) = 1$ value does not correspond to a physical pole, but the Pomeranchuk trajectory P_1 continued with an estimated slope should give a Regge pole at s_r, where $\mathrm{Re}\, a_{T=0}(s_r) = 2$.

Recently, this slope has been estimated to be $a'_{P_1}(0) \approx 1/80 m_\pi^2$ obtained by measuring the shrinkage in p-p elastic scattering diffraction peaks from 7 to 20 BeV/c incident momenta.[21] However, no similar shrinkage was seen in the case of $\pi^{\pm}$-p scattering.

Thus, if the Regge singularities are confined to simple poles and if a constant slope of Regge trajectories is assumed over a wide energy range, then a $\pi\pi$ resonance near 1250 MeV with the quantum numbers of T = 0 and J = 2 may be interpreted as the physical manifestation of P_1.

A second Pomeranchuk trajectory P_2 (T = 0, J parity even) with the intercept value estimated[22] to be $a_{P_2}(0) \approx 0.5$ has been recently postulated.[22,23] Under the above assumptions, this should manifest itself as a T = 0, J = 2 $\pi\pi$ resonance near 1800 MeV, which is above the phase-space limitations of this experiment.

IV. EXPERIMENTAL RESULTS

In reaction (a) $\pi^- + p \rightarrow \pi^- + \pi^+ + n$, the pion-pion and pion-nucleon final states have the following scattering amplitude decompositions in terms of isotopic spin:

$$A(\pi^-, \pi^+) = 1/3 \; A(0) + 1/2 \; A(1) + 1/6 \; A(2) \, , \qquad\qquad 1(a)$$

$$A(\pi^-, n) = 1 \; A(3/2) \, , \qquad\qquad 2(a)$$

$$\text{and} \qquad A(\pi^+, n) = 1/3 \; A(3/2) + 2/3 \; A(1/2) \, . \qquad\qquad 3(a)$$

Similarly, in reaction (b) $\pi^- + p \rightarrow \pi^- + \pi^0 + p$, we have

$$A(\pi^-, \pi^0) = 1/2 \; A(1) + 1/2 \; A(2) \, , \qquad\qquad 1(b)$$

$$A(\pi^0, p) = 2/3 \; A(3/2) + 1/3 \; A(1/2) \, , \qquad\qquad 2(b)$$

$$\text{and} \qquad A(\pi^-, p) = 1/3 \; A(3/2) + 2/3 \; A(1/2) \, . \qquad\qquad 3(b)$$

It should be noted that any $T = 0$ pion-pion resonance can be isolated by observing the effect in the state 1(a) and not in 1(b).

A. Effective-Mass Spectrum of the Pion-Pion System

Figures 16 (a) and (b) show the histogram of the dipion effective mass ω, for the (π^-, π^+) and (π^-, π^0) states, respectively. The (π^-, π^0) spectrum is strongly peaked at $\omega_r = 775$ MeV, which accounts for the ρ^- meson. The dashed curve in Fig. 16(b) represents the sum of 50% invariant phase space and 50% invariant phase space with a normalized Breit-Wigner resonance term of the form $N/[(\omega - \omega_r)^2 + (\Gamma/2)^2]$. The resonance term used has a value of full-width-at-half-maximum $\Gamma = 125$ MeV. This curve is normalized to the ρ^- peak.

The (π^-, π^+) spectrum is also strongly peaked at a central value of $\omega_r = 775$ MeV, which accounts for the ρ^0 meson; however, here the resonance width appears to be broader than the width of the ρ^- meson. With the mixture of invariant phase space and phase space with resonance, determined by the ρ^- meson spectrum, the dashed curve in Fig. 16(a) is computed by using a value of $\Gamma = 175$ MeV. This curve fits best around the ρ^0 region and is normalized to the ρ^0 peak. Both dashed curves are presented for a qualitative consideration.

A second peak in the (π^-, π^+) spectrum is observed with a central value of $\omega_r = 1250$ MeV and a width of $\Gamma \approx 200$ MeV. Similar peaks have been seen in recent experiments.[10,11,24] The shoulder seen around 1050 MeV, which appeared to be resolved at an earlier stage of this experiment, has lost its resolution in this final analysis.
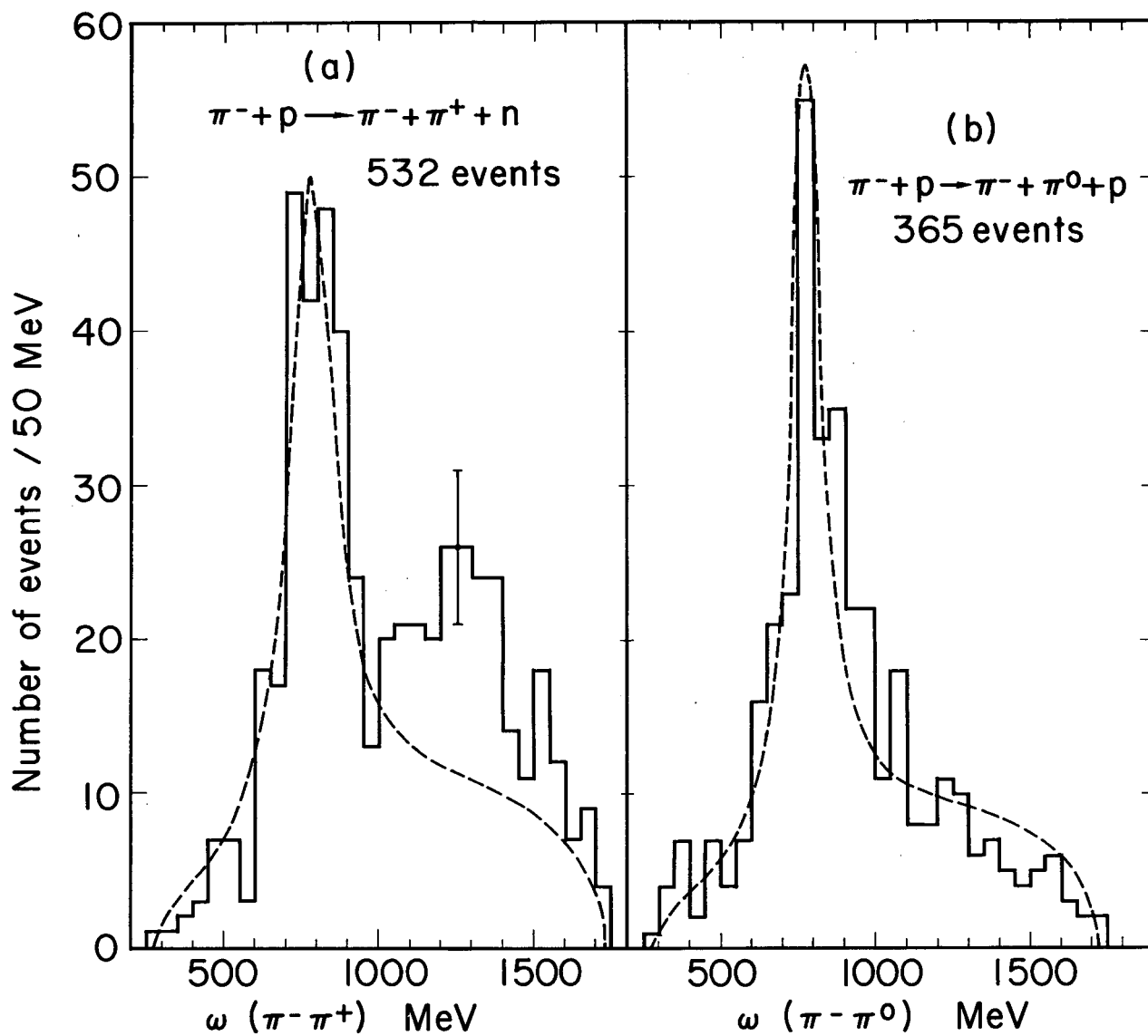
Fig. 16. (a) Spectrum of $\omega(\pi^-, \pi^+)$ from 532 events of reaction
$\pi^- + p \rightarrow \pi^- + \pi^+ + n$. Dashed curve: 50% invariant
phase-space and 50% invariant phase-space with Breit-
Wigner resonant term using Γ_r = 175 MeV, ω_r = 775 MeV.
(b) Spectrum of $\omega(\pi^-, \pi^0)$ from 365 events of reaction
$\pi^- + p \rightarrow \pi^- + \pi^0 + p$. Dashed curve: same as in (a)
with Γ_r = 125 MeV, and ω_r = 775 MeV.

MUB-1683

B.   Momentum Transfer to the Nucleon Distributions

Figures 17 (a) and (b) show the momentum transfer to the nucleon distribution for both reactions over the entire available ω region.   The lower solid curve in Fig. 17(a) represents the phase-space distribution $d\rho(t)/dt$, discussed earlier.

If we assume that the Chew-Low equation is valid in the t physical region for small values of t, and further assume a constant $\pi\pi$ cross section over a wide range in $s = \omega^2/m_\pi^2$, then an integration of this equation over s gives

$$\frac{\partial \sigma_{\pi^- p}(t)}{\partial t} = \frac{f^2}{2\pi} \frac{t}{(t+1)^2} \frac{m_{\pi^-}^2}{q_{1L}^2} \frac{\overline{\sigma}_{\pi\pi}}{2} \int_4^{s_{max}(t)} (s^2 - 4s)^{1/2} \, ds .$$

The dashed curve in Fig. 17(a) represents this distribution.

Finally, the top solid curve shows a simple $\sim t/(t+1)^2$ dependence of the data.   All three curves have been normalized over the entire experimental distribution area.

Figures 18 (c), (d) and (f) show the t distribution around the region of the observed resonances $700 < \omega(\pi^-, \pi^{+, 0}) < 850$ MeV and $1150 < \omega(\pi^-, \pi^+) <$ 1400 MeV.   In Figs. 18 (e) and (f) the first bin in the t distributions is relatively depleted.   This is caused by the phase-space limitations at these ω regions (see Fig. 15).

In all of these distributions, we note that most of the events are confined to values below t = 25, the rest being dispersed in a tail extending to t_{max} = 275.   This observation of strong enhancement at small t values is consistent with the suggested one-pion-exchange mechanism for the studied reactions.
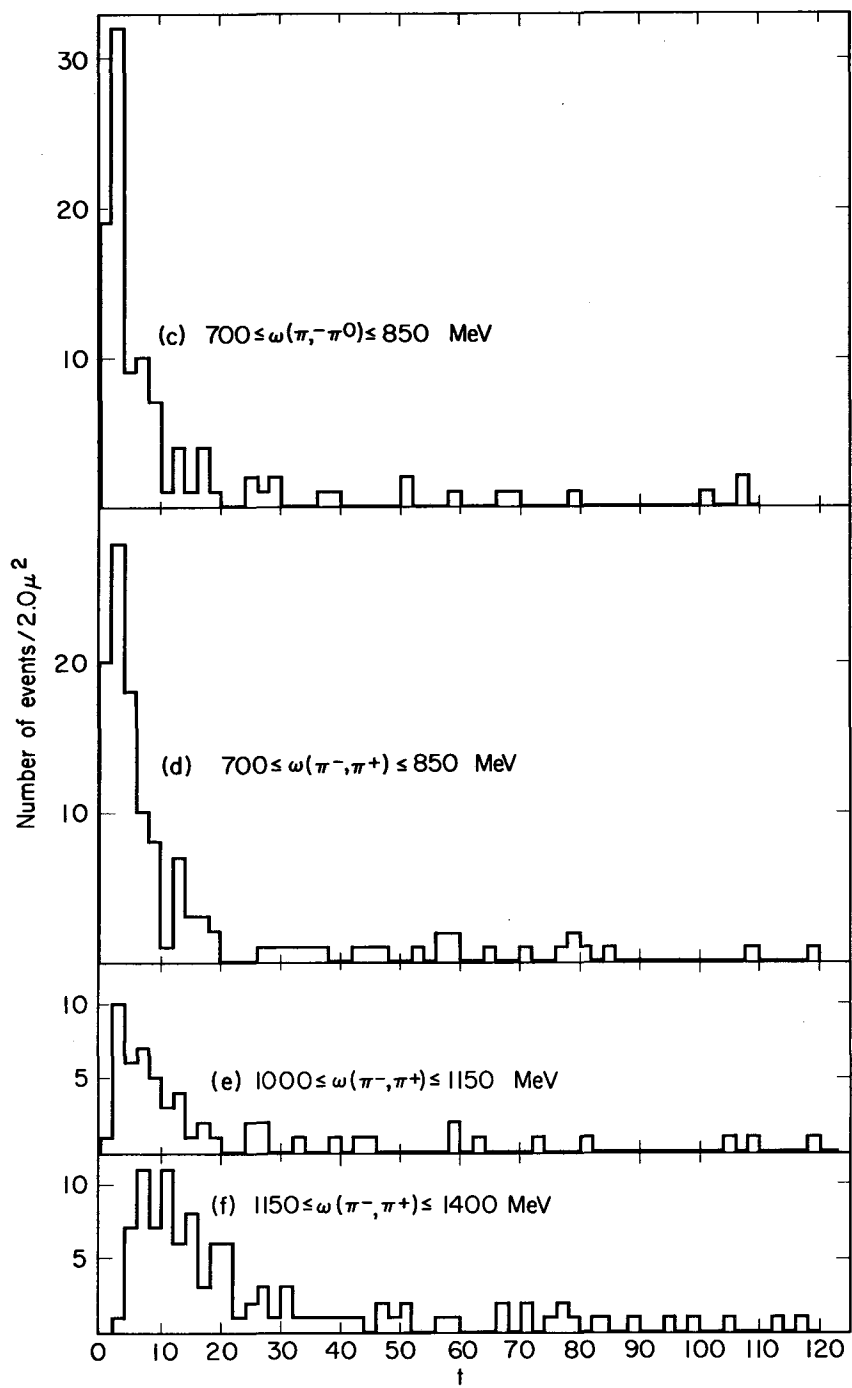
C.   Trieman-Yang Test for the One-Pion-Exchange Mechanism

Trieman and Yang suggested a method to test the one-pion-exchange interaction mechanism.[14]   In particular, they observe that since the exchanged particle in the interaction is spinless, there should not be any correlation in the rest frame of the incident pion between the plane defined by the final pions and the plane defined by the initial and final nucleon.   This implies that distributions in γ_{TY} (the previously defined Trieman-Yang angle) should be isotropic so long as the above interaction mechanism dominates.
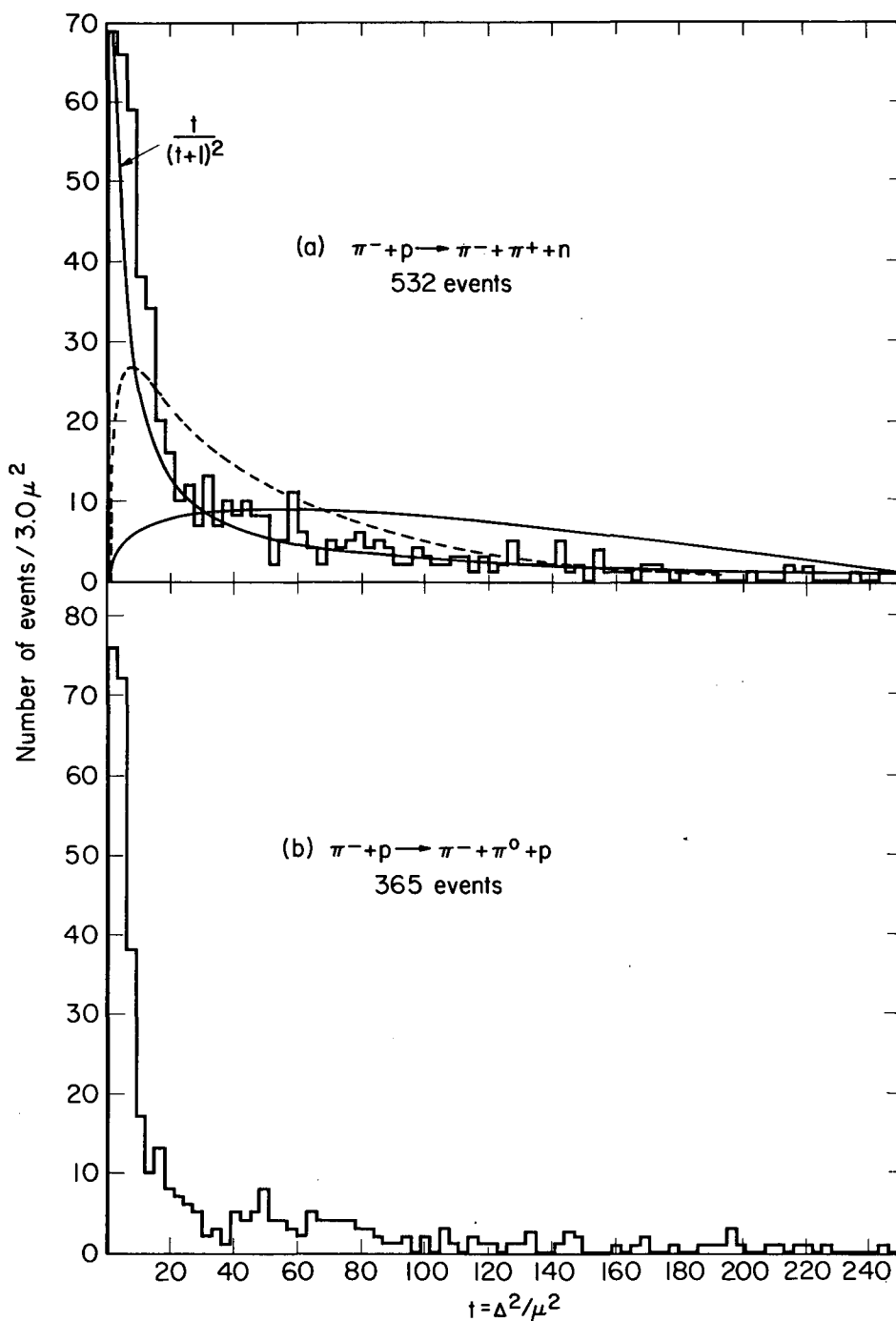
Fig. 17.   Distributions in t, the momentum transfer to the
nucleon over the entire ω range for the reactions (a)
and (b) as indicated.

MUB-1695

(c) $700 \leq \omega(\pi,-\pi^0) \leq 850$ MeV

(d) $700 \leq \omega(\pi^-,\pi^+) \leq 850$ MeV

(e) $1000 \leq \omega(\pi^-,\pi^+) \leq 1150$ MeV

(f) $1150 \leq \omega(\pi^-,\pi^+) \leq 1400$ MeV

MUB-1696

Fig. 18. Distributions in t over the indicated dipion
effective-mass regions.

Figure 19 shows the distribution in γ_{TY} as a function of t, for all events of reaction (a) and (b). By assuming parity conservation in strong interactions, the distributions are folded about the 0- to 180-deg line. Figure 19(f) shows that a marked anisotropy is obtained in reaction (b) at the t range of 25 < t < 275. In reaction (a) at the range of 9 < t < 20, the χ^2 value for isotropy is 8.5 with the corresponding probability being 13%. This and Figs. 19 (a), (d) and (e) indicate that the data are consistent with isotropy up to values of $t \lesssim 20$.

D. Decay-Angular Distributions in the Pion-Pion System

In order to study the resonant behavior of the observed peaks, distributions are constructed in $\cos\theta_{\pi\pi}$ for several segments of the ω spectrum of both states, where the decay angle $\theta_{\pi\pi}$ is the angle between the incoming and outgoing π^- evaluated in the barycentric system of final pions.

Due to the s vs t phase-space limitations, the angular distributions are presented with lower limits of t, which are $t_{min} \approx 0$ for the range of 275 < ω < 1000 MeV, and t_{min} = 4.0 for 1000 < ω < 1450 MeV. And, based on the above results, the angular distributions are constrained with an upper limit of t_{max} = 20.0 in order to obtain events which react predominantly via the one-pion-exchange mechanism.

The generalized Pauli principle for spinless bosons requires that $(-1)^{J+T}$ = even, under the exchange of both particles, where J and T are the orbital-angular momentum and isotopic-spin quantum numbers. Therefore, for the (π^-, π^0) state, the symmetrized isotopic-spin amplitudes of Eq. 1(b) have the following partial-wave expansions:
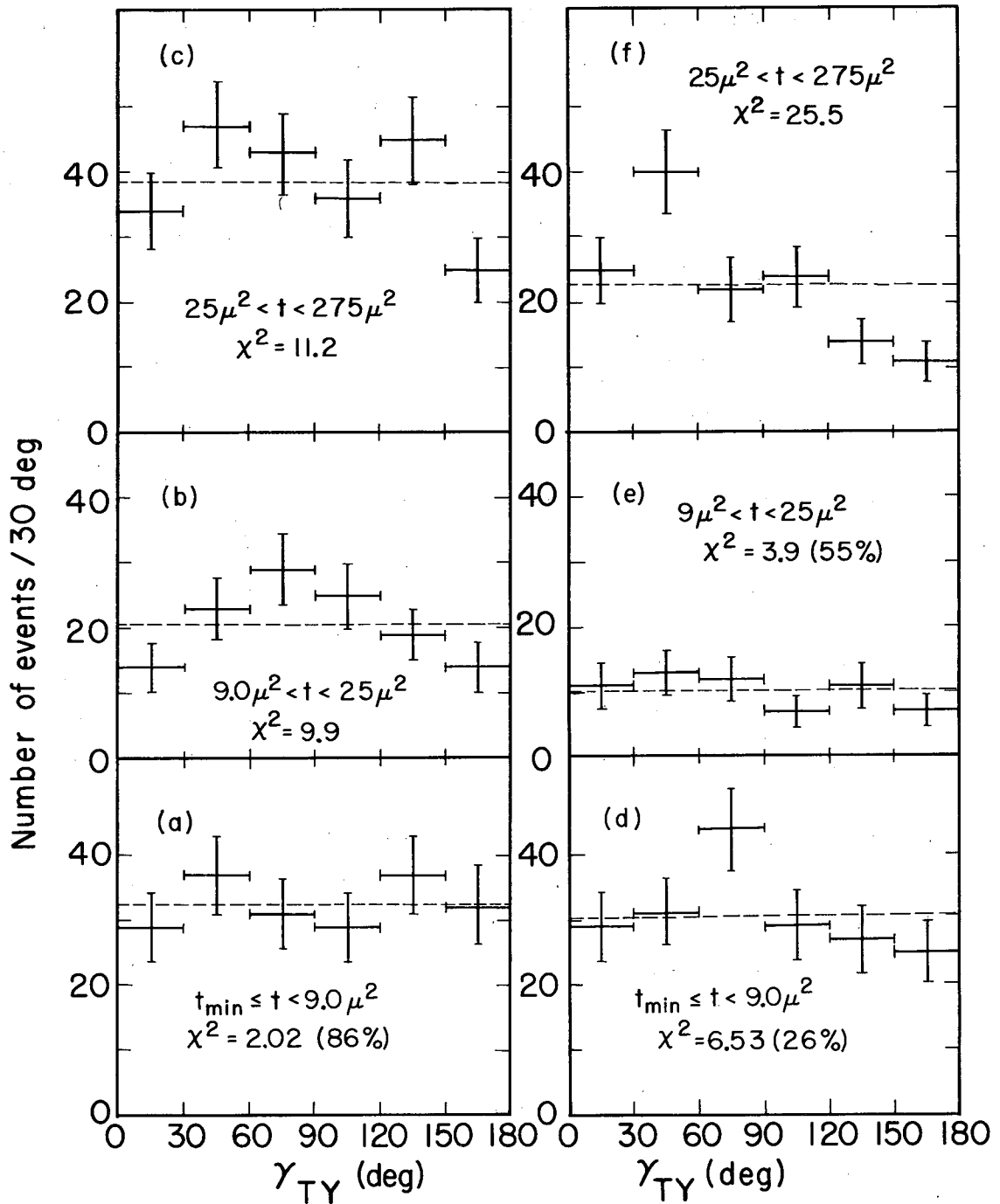
$$A_1(s, \theta_{\pi\pi}) = 2 \sum_{odd\ J} (2J + 1)\ e^{i\delta_J^1}\ \sin\delta_J^1\ P_J(\cos\theta_{\pi\pi})$$

and

$$A_2(s, \theta_{\pi\pi}) = 2 \sum_{even\ J} (2J + 1)\ e^{i\delta_J^2}\ \sin\delta_J^2\ P_J(\cos\theta_{\pi\pi}).$$

Assuming real S and P waves only, the differential cross section for the process $\pi^- + \pi^0 \rightarrow \pi^- + \pi^0$ becomes

Fig. 19. Trieman-Yang angular distributions, (a), (b), and
(c) are for the reaction $\pi^- + p \rightarrow \pi^- + \pi^+ + n$, (d), (e),
and (f) are for the reaction $\pi^- + p \rightarrow \pi^- + \pi^0 + p$; the
considered t ranges and the obtained χ^2 values for
isotropy are indicated.

$$\frac{d\sigma_{\pi^- \pi^0}}{d(\cos \theta_{\pi\pi})} = 2\pi\lambda^2 \left| 1/2 \, A_1(s, \theta_{\pi\pi}) + 1/2 \, A_2(s, \theta_{\pi\pi}) \right|^2$$

$$= 2\pi\lambda^2 [9 \sin^2 \delta_1^1 \cos^2 \theta_{\pi\pi} + 6 \sin \delta_1^1 \sin \delta_0^2 \cos (\delta_1^1 - \delta_0^2) \cos \theta_{\pi\pi} + \sin^2 \delta_0^2].$$

The Forward-Backward asymmetry resulting from interference between both outgoing S and P waves, is then of the form

$$A = \frac{F - B}{F + B} = \frac{6 \sin \delta_1^1 \sin \delta_0^2 \cos (\delta_1^1 - \delta_0^2)}{9 \sin^2 \delta_1^1 \sin^2 \delta_0^2} \, .$$

Figure 20(h) is the decay-angular distribution at the ρ^- resonance, showing a characteristic $\cos^2 \theta_{\pi\pi}$ dependence over a constant background. Figures 20 (g) and (i) are the angular distributions before and after the ρ^- resonance, respectively. It is seen that the forward-backward asymmetry A, has a value near zero, before and at the ρ^- resonance, which becomes large and positive just after the resonance region. This indicates that the P-wave phase shift δ_1^1 has crossed over 90 deg at $700 < \omega(\pi^-, \pi^0) < 850$ MeV, and the T = 2 S-wave phase shift δ_0^2 must be small and negative; which implies that the T = 2 S-wave state is repulsive.

Figure 20(b) shows that the angular distribution at the ρ^0 resonance is strongly asymmetric in the forward direction. This behavior continues after the ρ^0 resonance, as seen in Fig. 20(c). The forward asymmetry in the decay-angular distribution at the ρ^0 indicates that an S-wave or a D-wave phase shift from the isotopic spin T = 0 component of the (π^-, π^+) state, $(\delta_0^0$ or $\delta_2^0)$, is sufficiently strong to interfere with the P-wave phase shift of the T = 1 component, δ_1^1, such that the effective phase shift $(\delta_1^1 - \delta_0^0)$ or $(\delta_1^1 - \delta_2^0)$ is prevented from reaching 90 deg at the ρ^0 resonance. The T = 2 component in the (π^-, π^+) state is ruled out for such a strong interference behavior since it should have appeared in both reactions. The above discussion becomes explicit by the following.

Assuming real S, P, and D waves only, in the partial wave expansions of the isotopic-spin amplitudes of Eq. 1(a), the differential cross section for the process $\pi^- + \pi^+ \to \pi^- + \pi^+$ can be written as
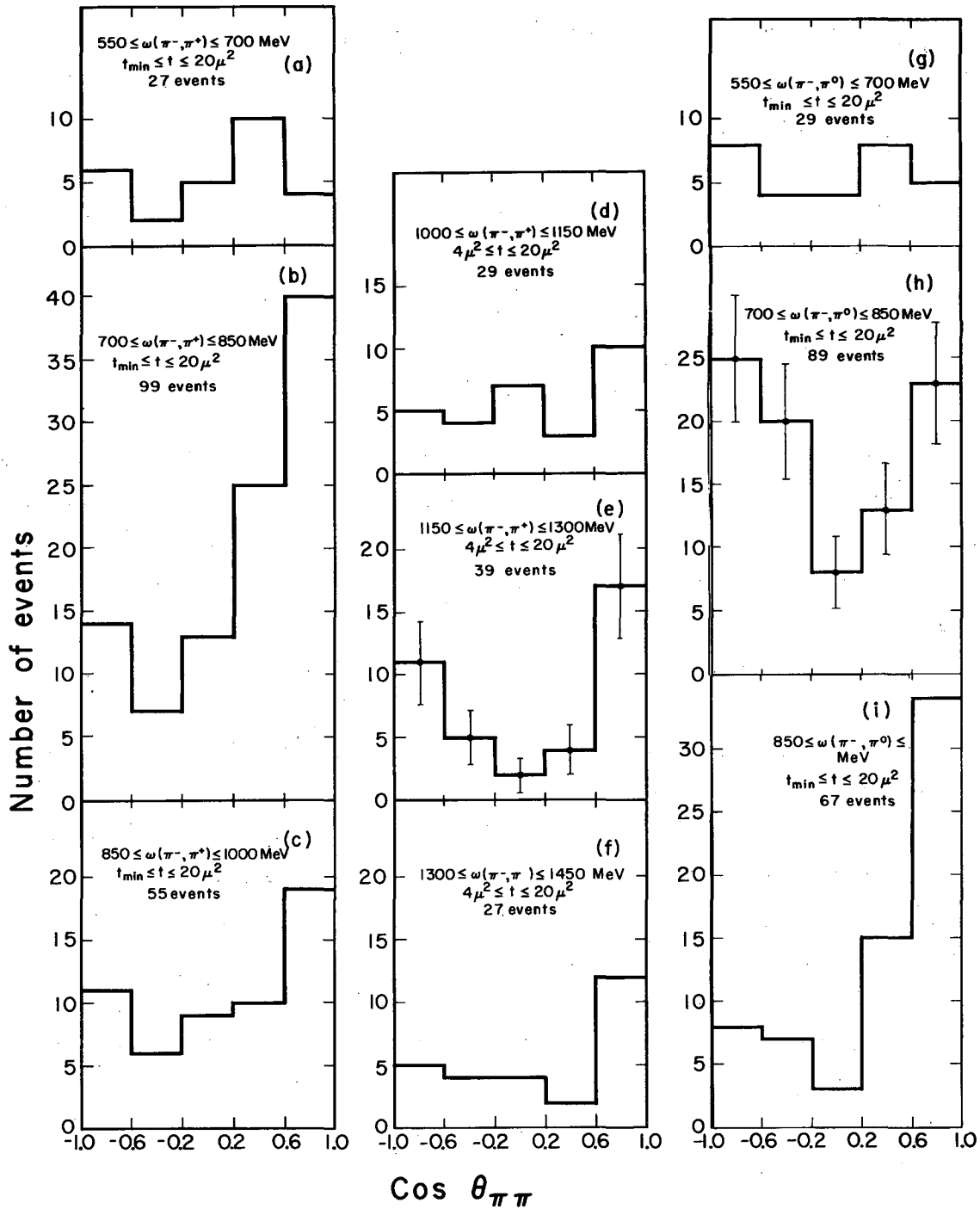
Fig. 20. Distributions in cos $\theta_{\pi\pi}$, the angle between the incoming and outgoing π^- in the barycentric system of the final pions, for the indicated $\pi\pi$ states and ω, t intervals.

$$\frac{d\sigma_{\pi^-\pi^+}}{d(\cos\theta_{\pi\pi})} = 2\pi\lambda^2 \left| 1/3\, A_0(s,\theta_{\pi\pi}) + 1/2\, A_1(s,\theta_{\pi\pi}) + 1/6\, A_2(s,\theta_{\pi\pi}) \right|^2$$

$$= 2\pi\lambda^2 \left[A + B\cos\theta_{\pi\pi} + C\cos^2\theta_{\pi\pi} + D(3\cos^2\theta_{\pi\pi} - 1) + \right.$$

$$\left. E(3\cos^2\theta_{\pi\pi} - 1)\cos\theta_{\pi\pi} + F(3\cos^2\theta_{\pi\pi} - 1)^2 \right]$$

where the necessary odd powers in $\cos\theta_{\pi\pi}$ are obtained to describe the forward asymmetry in the ρ^0 decay-angular distribution.

For completeness, we specify the above coefficients necessary to determine the phase shifts in an experiment with higher statistics and better resolution. With the phase-shift indices denoted as δ_J^T we have

$$A = 4/9\,\sin^2\delta_0^0 + 1/9\,\sin^2\delta_0^2 + 4/9\,\cos(\delta_0^2 - \delta_0^0)\sin\delta_0^2\sin\delta_0^0,$$

$$B = 4\cos(\delta_0^0 - \delta_1^1)\sin\delta_0^0\sin\delta_1^1 + 2\cos(\delta_0^2 - \delta_1^1)\sin\delta_0^2\sin\delta_1^1,$$

$$C = 9\sin^2\delta_1^1,$$

$$D = 20/9\,\cos(\delta_2^0 - \delta_0^0)\sin\delta_2^0\sin\delta_0^0 + 10/9\,\cos(\delta_2^2 - \delta_0^0)\sin\delta_2^2\sin\delta_0^0$$

$$+ 10/9\,\cos(\delta_0^2 - \delta_2^0)\sin\delta_0^2\sin\delta_2^0 + 5/9\,\cos(\delta_2^2 - \delta_0^2)\sin\delta_2^2\sin\delta_0^2,$$

$$E = 10\cos(\delta_2^0 - \delta_1^1)\sin\delta_2^0\sin\delta_1^1 + 5\cos(\delta_2^2 - \delta_1^1)\sin\delta_2^2\sin\delta_1^1,$$

and

$$F = 25/9\,\sin^2\delta_2^0 + 25/36\,\sin^2\delta_2^2 + 25/9\,\cos(\delta_2^2 - \delta_2^0)\sin\delta_2^2\sin\delta_2^0.$$

Here we have $\lambda = \hbar c/q$, where q is the decay-pion momentum in the rest frame of the ρ, and $q^2 = \omega^2/4 - m_{\pi^-}^2$. Assuming an interaction radius of one pion-Compton-wavelength, at $\omega = 775$ MeV the maximum orbital-angular momentum is $J_{max} \sim \lambda_\pi/\lambda = 2.6$ so that the above partial-wave decomposition is suitable.

Figures 20 (d), (e), and (f) show the angular distribution before the peak $1000 \leqslant \omega(\pi^-,\pi^+) < 1150$ MeV, at the 1250-MeV peak $1150 \leqslant \omega(\pi^-,\pi^+) < 1300$ MeV, and after the peak $1300 \leqslant \omega(\pi^-,\pi^+) < 1450$ MeV, respectively. We note that Fig. 20(e) is a nonisotropic symmetric distribution. The 1250-MeV peak is seen in the (π^-,π^+) state and not in the (π^-,π^0), so that this resonance has isotopic spin $T = 0$, whereby it is confined to have an even angular-momentum

value. Although Fig. 20(e) does not show the characteristic D-wave hump at $\theta_{\pi\pi}$ = 90 deg, the J = 0 value is ruled out by nonisotropy.

To conclude this section, we note that the striking difference in the decay-angular distribution between the ρ^0 and ρ^- needs further examination. This difference seems to be independent of the reaction c.m. energy. If the apparent enlarged width[25] of the ρ^0 is due to an adjacent ω^0 production which decays electromagnetically[26] into two pions (as it has been assumed elsewhere[27]), then interference with this same process cannot explain the forward asymmetry in the ρ^0 decay-angular distribution. This is because the general form for the angular distribution of a vector particle decaying into two pions, when averaged over the azimuthal angle ϕ, is of the form[28] A + B $\cos^2\theta_{\pi\pi}$ whether the mechanism is strong or electromagnetic. The azimuthal angle ϕ is measured with respect to the normal to the ρ^0 or ω^0 production plane.

However, by assuming that the observed forward asymmetry is strictly due to some $\pi\pi$ effect, the ρ^0 decay-angular distribution could be explained by the interference of a nearby resonance in the T = 0 and J^{PG} state of 0^{++} or 2^{++}.

E. ρ^0 and ρ^- Production Angular Distribution

Assuming ρ production proceeds via the one-pion-exchange mechanism, and taking account of the resonance spin, S. Berman[29] has computed the ρ-production differential cross section in the reaction c.m. system. This is of the form

$$\left(\frac{d\sigma}{d(\cos\theta_\rho)}\right)_{c.m.} = 2\pi \frac{g^2_{\pi NN}}{4\pi}\frac{g^2_{\pi\pi\rho}}{4\pi}\frac{t}{(t+m_\pi^2)^2}\frac{P_\rho}{P_\pi}\frac{[t+(m_\rho+m_\pi)^2][t+(m_\rho-m_\pi)^2]}{4m_\rho^2 W^2},$$

where the coupling constants are

$$\frac{g^2_{\pi NN}}{4\pi} \approx 15.0 \qquad \text{and} \qquad \frac{g^2_{\pi\pi\rho}}{4\pi} = \frac{12\,\Gamma_{\rho\pi\pi}}{m_\rho[1-4m_\pi^2/m_\rho^2]^{3/2}},$$

and where $t = -(P_\pi - P_\rho)^2$ is the momentum transfer between the incident π^- and the ρ meson. Evaluating this in the reaction c.m. system we obtain

$$t = 2(E_\pi E_\rho - P_\pi P_\rho \cos\theta_\rho) - m_\pi^2 - m_\rho^2$$

where

$$p_\rho^2 = \frac{[W^2 + M_n - m_\rho^2]^2 - 4M_n^2 W^2}{4W^2} \quad \text{and} \quad p_\pi^2 = \frac{[W^2 + M_p^2 - m_\pi^2]^2 - 4M_p^2 W^2}{4W^2}.$$

Here, W is the reaction c.m. total energy.

Figures 21 (a) and (b) show the ρ^0 and ρ^- production angular distributions, respectively. Both distributions are strongly peaked in the forward direction.

Since the above equation used directly does not reproduce the experimental angular distribution, an overall form factor $F^2(t)$ is introduced which multiplies this equation. Choosing a one-parameter form factor as $F(t) = (m_0^2 - m_\pi^2)/(m_0^2 + t)$, which has the normalization of $F(-m_\pi^2) = 1$, a fit is performed for each distribution. Because the experimental distributions are not given in terms of cross sections, a second parameter N_0 is introduced which normalizes the fit to the entire distribution areas.

The curves in Figs. 21 (a) and (b) are the result of such fits, reproducing the experimental distribution with the adjusted parameter value of $m_0 = (2.3 \pm 0.5)m_\pi$.

The use of more than one-parameter form factors, specifically for the $\pi\pi\rho$ and πNN vertices, was not found to be practical, since the experimental distributions were not given in terms of cross sections.

F. Dalitz Plots and Projections

Dalitz plots are constructed for both reactions of interest in terms of the final pion-reaction center-of-mass kinetic energies, T_π. Figure 22 shows the Dalitz plot for the reaction $\pi^- + p \rightarrow \pi^- + \pi^+ + n$. The lines of constant dipion mass are obtained from the relation $T_3 + T_4 = [(\omega^2 + W^2 - M_2^2) \div 2W] - m_3 - m_4$, where the indices 3 and 4 are for the final pions and 2 for the recoil nucleon; these are indicated on top of the Dalitz envelopes.

The top and left projections in terms of T_{π^-} and T_{π^+} are equivalent to the (π^+, n) and (π^-, n) effective mass spectra, respectively. The curves shown in these projections are the invariant phase-space integrals normalized to the total area of each histogram. The position of possible pion-nucleon resonances in each final state are indicated accordingly. No appreciable deviation from phase space is seen in either state.
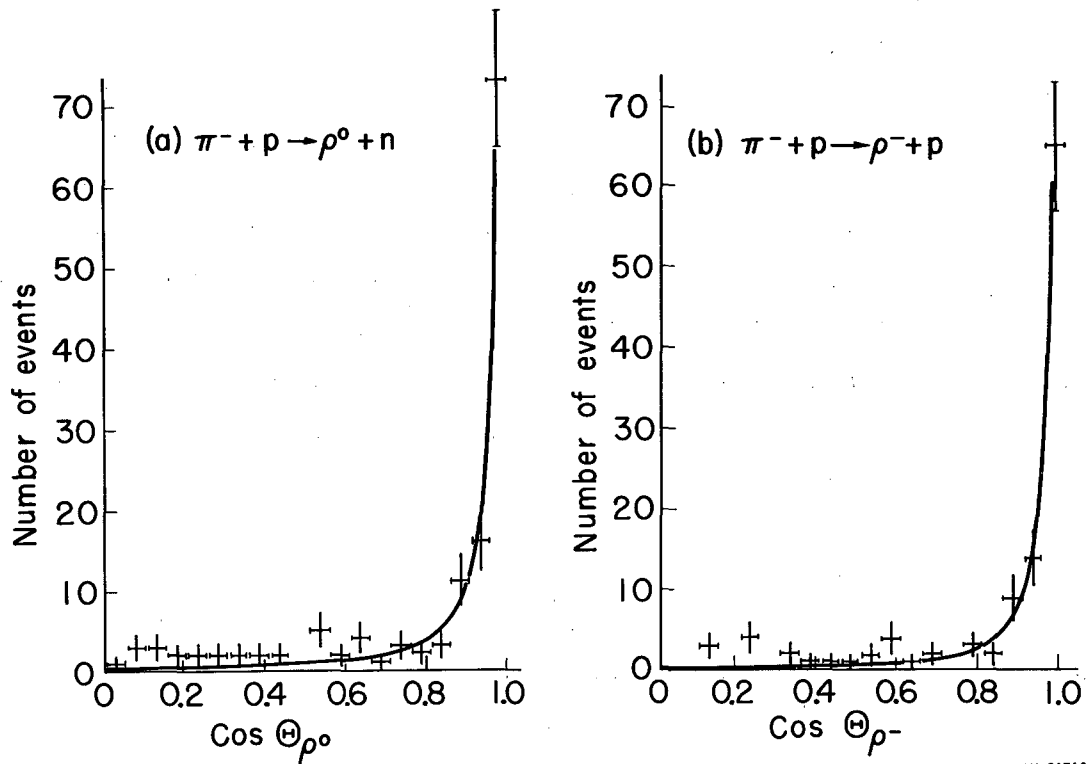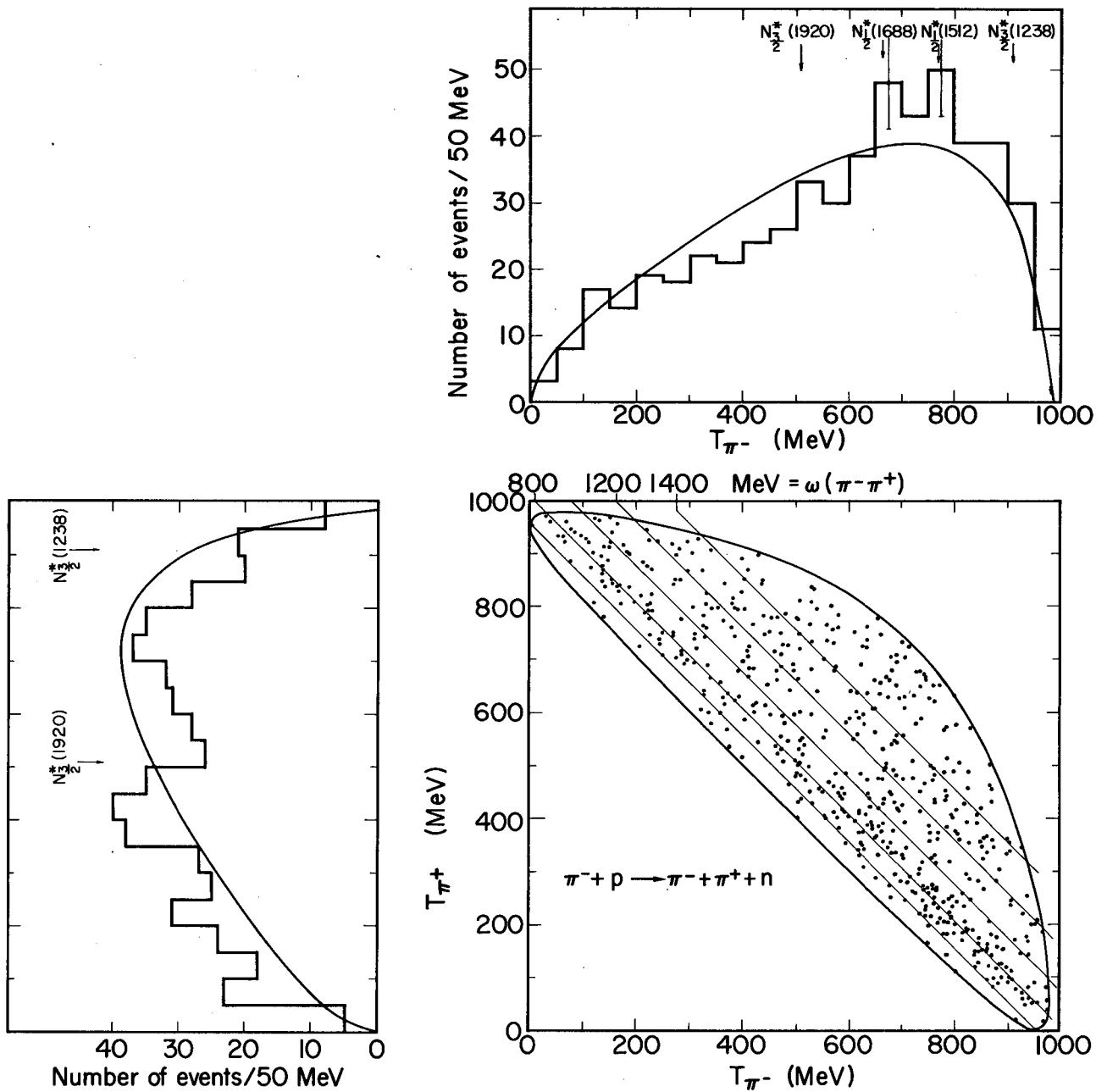
Fig. 21. (a) ρ^0 production angular distribution in the c. m.
system of reaction $\pi^- + p \rightarrow \rho^0 + n$, (b) ρ^- production
angular distribution in the c. m. system of reaction
$\pi^- + p \rightarrow \rho^- + p$. Curves are the best fit to the data
assuming a form factor, a ρ spin factor evaluated in
the physical region, and the one-pion-exchange
mechanism.

Fig. 22. Dalitz plot for the reaction $\pi^- + p \rightarrow \pi^- + \pi^+ + n$, in terms of final-pion c.m. kinetic energies. Top projection in T_{π^-} represents the (π^+, n) state, left projection in T_{π^+} represents the (π^-, n) state; with curves showing the phase-space distribution. Arrows indicate positions of possible N^* resonances.

Figure 23 is the Dalitz plot for the reaction $\pi^- + p \rightarrow \pi^- + \pi^0 + p$. Here, the top and left projections in terms of T_{π^-} and T_{π^0} are equivalent to the (π^0, p) and (π^-, p) effective mass spectra, respectively. Deviations from phase space are evident in both states.

The T_{π^0} distribution has a 4-standard-deviation peak corresponding to 2400-MeV (π^-, p) effective mass. The T_{π^-} distribution has a 3.5-standard-deviation peak at the $N^*_{3/2}(1238)$ position. If the peak in the T_{π^-} distribution is assumed to be due to the $N^*_{3/2}(1238)$ resonance, then the 2400-MeV peak in the T_{π^0} distribution must be considered as spurious. An examination of the Dalitz plot shows that 40% of the events at the 2400-MeV region of T_{π^0} come from the $N^*_{3/2}(1238)$ of T_{π^-}, and 25% from the ρ^- resonance.

It could be said that in the first reaction the final-state $\pi\pi$ resonances dominate over (π, n) interactions, whereas in the second reaction, with the presence of a single $\pi\pi$ resonance, the remaining phase space is available to the pions for any (π, p) interactions.

Recently, however, a model of N^* production has been given,[30] with which the above results are in agreement in so far as they can be tested. This treatment is based on the model that isobar production predominantly proceeds via a vector-meson exchange, which in our case would be the ρ meson. Specific predictions of this model that are applicable to the final states of the studied reactions are the following:

(A) $N^*_{3/2}$ production in the $(\pi-, n)$ state is strictly forbidden, even though this state has the largest $T = 3/2$ projection [see Eq. 2(a)]. The $N^*_{3/2}$ production is dominant in the (π^0, p) state with a ratio of 4:1 as compared to the (π^-, p) and (π^+, n) final states [see Eqs. 2(b), 3(b) and 3(a)].

(B) With the energy-momentum assignment of

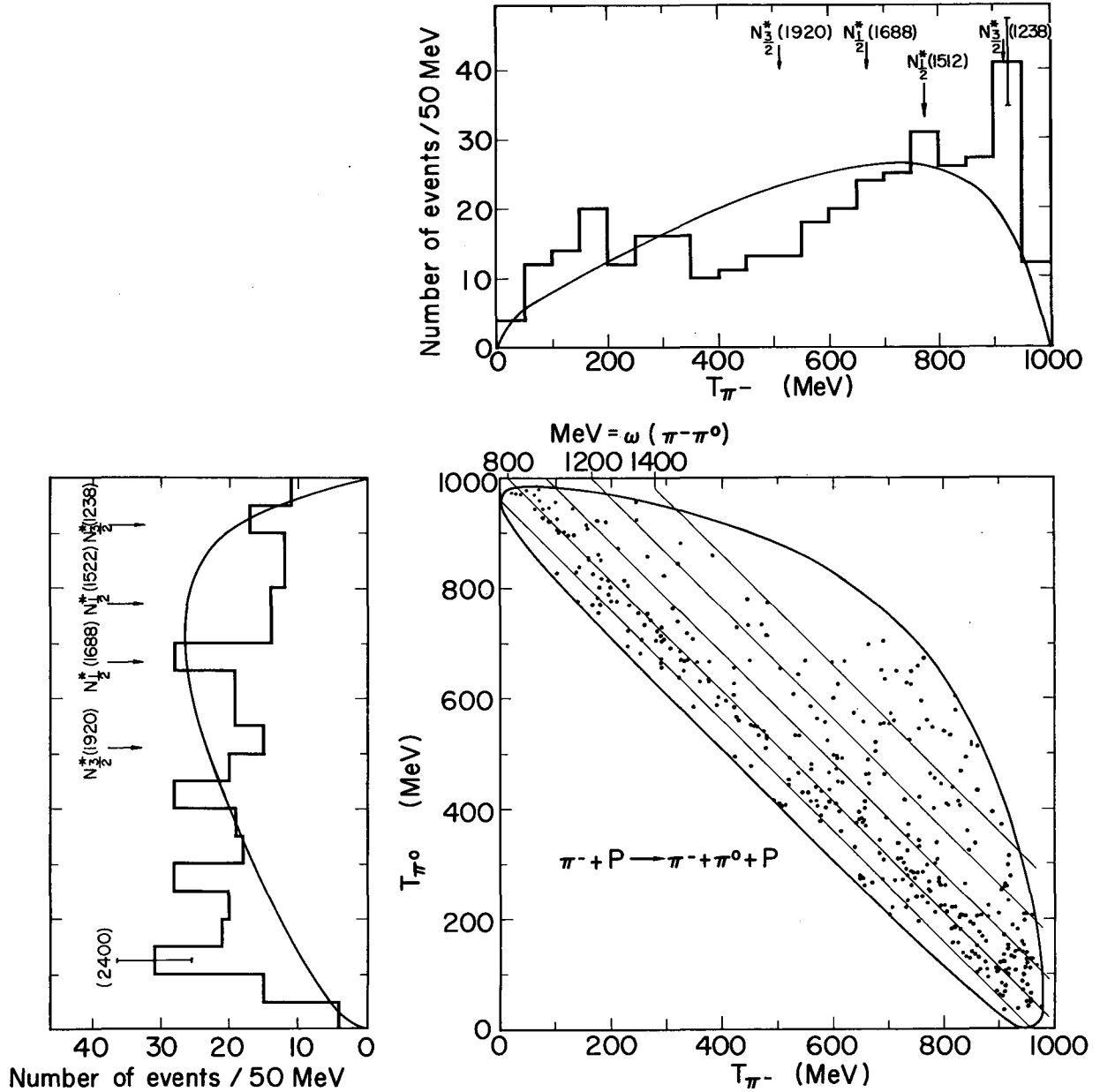$$\pi^- + p \rightarrow \left(\begin{array}{c} N^* \\ N + \pi \end{array} \right) + \pi$$

as

$$q_1 + p_1 \rightarrow p_2 + q_3 + q_4 ,$$

the decay-pion angular distribution in the rest frame of $N^*_{3/2}$ should be $1 + 3\cos^2\theta_{\pi N}$, where

$$\cos\theta_{\pi N} = \frac{q_3 \cdot (q_1 \times q_4)}{|q_3||q_1 \times q_4|} ,$$

and where all of the vectors are evaluated in the rest frame of the isobar.

Fig. 23. Dalitz plot for the reaction $\pi^- + p \to \pi^- + \pi^0 + p$,
in terms of final-pion c. m. kinetic energies. Top
projection in T_{π^-} represents the (π^0, p) state, left
projection in T_{π^0} represents the (π^-, p) state; with
curves showing the phase-space distribution. Arrows
indicate positions of possible N^* resonances.

Thus, $\theta_{\pi N}$ is the angle between the N^*-decay pion with respect to the normal of the N^*-production plane, evaluated in the isobar rest frame.

(C) Finally, Stodolsky and Sakurai propose a test for the one-vector-meson exchange mechanism, analogous to the Trieman-Yang test for the one-pion-exchange.[30] Defining a correlation γ_{SS}, where

$$\cos \gamma_{SS} = \frac{(q_1 \times q_4) \cdot [(q_1 - q_4) \times q_3]}{|q_1 \times q_4| |(q_1 - q_4) \times q_3|} ,$$

a distribution in $\cos \gamma_{SS}$ must be of the form

$$A + B \cos \gamma_{SS} + C \cos^2 \gamma_{SS}$$

if the one-vector meson-exchange mechanism is dominant.

This experiment is in agreement with the prediction in (A). Predictions (B) and (C) could not be tested due to limited statistics. However, a collaborative effort in progress, which consists of a similar study at 3.9- and 4.2-BeV π^- - p interactions, and high in statistics, should be able to answer to some of the questions of interest.

ACKNOWLEDGMENTS

FOOTNOTES AND REFERENCES

*Original version filed as Ph. D. thesis May 15, 1962; present version revised as UCRL Report August 13, 1963.

†Present address: Stanford University, Stanford Linear Accelerator Center, Stanford, California.

1. G. F. Chew and F. E. Low, Phys. Rev. 113, 1640 (1959).

2. W. R. Frazer and J. R. Fulco, Phys. Rev. 117, 1609 (1960); also W. R. Frazer, Dispersion Relations, edited by G. R. Screaton (Oliver and Boyd, Ltd., London, 1961) p. 254.

3. F. J. Bowcock, W. N. Cottingham, and D. Lurié, Phys. Rev. Letters 5, 386 (1960).

4. Duane Carmoney, The Pion-Pion Cross Section by the Chew-Low Method, Lawrence Radiation Laboratory Report UCRL 9886, Oct. 1961 (unpublished).

5. A. R. Erwin, R. March, W. D. Walker, and E. West, Phys. Rev. Letters 6, 628 (1961).

6. E. Pickup, D. K. Robinson, and E. O. Salant, Phys. Rev. Letters 7, 192 (1961).

7. G. F. Chew and S. C. Frautschi, Phys. Rev. Letters 7, 394 (1961), also 8, 41 (1962).

8. G. F. Chew, S. C. Frautschi, and S. Mandelstam, Phys. Rev. 126, 1202 (1962).

9. S. C. Frautschi, M. Gell-Mann, and F. Zachariasen, Phys. Rev. 126, 2204, (1962).

10. W. Selove, V. Hagopian, H. Brody, A. Baker, and E. Leboy, Phys. Rev. Letters 9, 272 (1962).

11. J. J. Veillet, J. Hennessy, H. Bingham, M. Bloch, D. Drijard, A. Lagarrigue, P. Mittner, A. Rousset, G. Bellini, M. di Corato, E. Fiorini, and P. Negri, Phys. Rev. Letters 10, 29 (1963).

12. H. S. White, Data Processing for Bubble Chambers, Lawrence Radiation Laboratory Report UCRL 9475, November 1960 (unpublished).

13. Reference Manual for FOG-CLOUDY-FAIR Bubble Chamber Data Processing System, Lawrence Radiation Laboratory Document UCID 1340 (unpublished).

14. S. M. Trieman and C. N. Yang, Phys. Rev. Letters 8, 140 (1962).

15. A FORTRAN calling subroutine for the computation of this angle was kindly supplied by Dr. William B. Johnson.

16. Alvarez Group Memo No. 334, Lawrence Radiation Laboratory, 1961. The author would like to thank Mr. Marcus Horovitz for kindly supplying the ATHOS 3-body phase-space program.

17. See for example S. D. Drell, Proc. Intern. Conf. High Energy Physics, CERN, p. 897, 1962. W. Kummer, CERN report 62-13.

18. T. Regge, Nuovo Cimento, 14, 951 (1959) and 18, 947 (1960).

19. G. F. Chew, The S-Matrix Theory of Strong Interactions (W. A. Benjamin and Co, New York, 1961).

20. B. M. Udgaonkar, Phys. Rev. Letters 8, 142 (1962).

21. K. J. Foley, S. J. Lindenbaum, W. A. Love, S. Ozaki, J. J. Russell, and L. C. L. Yuan, Phys. Rev. Letters 10, 376 (1963), and 10, 543 (1963).

22. K. Igi, Phys. Rev. Letters 9, 76 (1962), and K. Igi, Two Vacuum Poles and Pion-Nucleon Scattering, University of California, Berkeley preprint, 1963 (submitted to Phys. Rev.).

23. F. Hadjioannou, R. J. N. Phillips, and W. Rarita, Phys. Rev. Letters 9, 183 (1962).

24. L. Bondàr, K. Bongartz, M. Deutschmann, H. Weber, D. C. Colley, W. P. Dodd, J. Simmons, B. Tallini, J. Boebes, B. Nellen, G. Winter, E. Lohrmann, E. Raubold, G. Wolf, J. M. Brownlee, I. Butterworth, F. I. Campayne, M. Ibbotson, Y. S. Liu, N. N. Biswas, I. Derado, D. Lüers, G. Lütjens, and M. Schmitz, Physics Letters 5, 153 (1963).

25. For a discussion on the ρ width at a lower c.m. energy see Saclay-Orsay-Bari-Bolognia Collaboration, π⁻ - p Interactions at 1.59 GeV/c (preprint 1963), submitted to Nuovo Cimento.

26. J. Bernstein and G. Feinberg, Proc. Intern. Conf. High Energy Physics, CERN, 1962, p. 170.

27. W. J. Fickinger, D. K. Robinson, and E. O. Salant, Phys. Rev. Letters 10, 457 (1963).

28. The author would like to thank Dr. S. M. Berman and Dr. D. B. Lichtenberg (Stanford Linear Accelerator Center, Stanford University), for indication of this point, and for many related stimulating discussions.

29. S. M. Berman, Stanford Linear Accelerator Center (Stanford University), private communication, 1963.

30. L. Stodolsky (Enrico Fermi Institute for Nuclear Studies, University of Chicago), private communication, 1963, and L. Stodolsky and J. J. Sakurai, Phys. Rev. Letters $\underline{11}$, 90 (1963).